This is a preprint, the final version is subject to change, of the American Mineralogist (MSA)
Cite as Authors (Year) Title. American Mineralogist, in press.
(DOI will not work until issue is live.) DOI: http://dx.doi.org/10.2138/am-2016-5507

REVISION 1

Chromium, vanadium, and titanium valence systematics in solar system pyroxene as a recorder of oxygen fugacity, planetary provenance, and processes

James J. Papike[1], Steven B. Simon[2], Paul V. Burger[1,*], Aaron S. Bell[1], Charles K. Shearer[1], and James M. Karner[3]

[1]Institute of Meteoritics
Department of Earth and Planetary Sciences
University of New Mexico
Albuquerque, New Mexico 87131, U.S.A.

[2]Department of Geophysical Sciences
The University of Chicago
Chicago, Illinois 60637, U.S.A.

[3]Department of Earth, Environmental, and Planetary Sciences,
Case Western Reserve University
Cleveland, Ohio 44106, U.S.A.

*Correspondence author: pvburger@unm.edu

Submitted 10/30/15

This is a preprint, the final version is subject to change, of the American Mineralogist (MSA)
Cite as Authors (Year) Title. American Mineralogist, in press.
(DOI will not work until issue is live.) DOI: http://dx.doi.org/10.2138/am-2016-5507

ABSTRACT

Pyroxene is arguably the most powerful single phase geochemical and petrologic recorder of Solar System processes, from nebular condensation through planetary evolution, over a wide range of temperatures, pressures, and fO_2. It is an important mineral phase in the crusts and mantles of evolved planets, in undifferentiated and differentiated asteroids, and in refractory inclusions – the earliest solar system materials. Here, we review the valence state partitioning behavior of Cr (Cr^{2+}, Cr^{3+}), Ti (T^{i3+}, Ti^{4+}), and V (V^{2+}, V^{3+}, V^{4+}, V^{5+}) among crystallographic sites in pyroxene over a range of fO_2 from approximately fayalite-magnetite-quartz (FMQ) to ~7 log units below iron-wüstite (IW-7), and decipher how pyroxene can be used as a recorder of conditions of planetary and nebular environments and planetary parentage. The most important crystallographic site in pyroxene with respect to its influence on mineral/melt partitioning is M2; its Ca content has a huge effect on partitioning behavior, because the large Ca cation expands the structure. As a result, distribution coefficients (Ds) for Cr and V increase with increasing Ca content from orthopyroxene to pigeonite to augite. In addition, it is noted that V^{3+} is favored over V^{4+} in olivine and pyroxene. In pyroxene in refractory inclusions, Ti^{3+} is favored over Ti^{4+} and incorporation of Ti is facilitated by the high availability of Al for coupled substitution. The most important results from analysis of pyroxene in martian meteorites (e.g. QUE 94201) are the oxygen fugacity estimates of IW+0.2 and IW+0.9 derived from partitioning and valence data for Cr and V, respectively, obtained from experiments using appropriate temperatures and melt compositions. In angrites, changes in V valence state may translate to changes in fO_2, from IW-0.7 during early pyroxene crystallization, to IW+0.5 during later episodes of pyroxene crystallization. In addition to fO_2, the partitioning behavior of Cr, V and Ti between pyroxene

and melt is also dependent upon availability of other cations, especially Al, for charge-balancing coupled substitutions.

INTRODUCTION

This is a comparative planetary mineralogy review emphasizing the valence-state partitioning behavior of Cr, V, and Ti between the pyroxene M1 and M2 sites and coexisting equilibrium melt over the oxygen fugacity range from the fayalite-magnetite-quartz (FMQ) buffer to approximately seven log units below the iron-wüstite buffer (~IW-7). We focus primarily on pyroxenes from planetary basalts, as they record fundamental igneous mineral-melt processes that have occurred on the Moon, Mars, Earth, and small planetary bodies (e.g. angrite and eucrite parent bodies) from ~4.5 Ga to the present time.

Some lithophile elements can have more than one oxidation state under conditions relevant to the formation of planetary materials. The oxygen fugacities at which important lithophile elements have multiple valences and the environments in which they occur are summarized in Figure 1. Changing the valence of an element affects its ionic radius, which affects its compatibility in a given crystallographic site and its partitioning behavior into a given mineral. The range of the ionic radii of the cations considered here is illustrated in Figure 2. Understanding the fundamental interactions between the behavior of multivalent cations and a mineral structure is critical to deciphering the fO_2 of a planetary body and fingerprinting planetary parentage. This crystal chemical approach has led to the development of several "valence state oxybarometers," such as a semi-quantitative V-valence spinel oxybarometer (Papike et. al. 2004); a V-valence glass oxybarometer (Sutton et al. 2005, Karner et al. 2006); and a Cr- and V-valence pyroxene oxybarometer (Karner et al. 2007a,b; 2008). Papike et al.

(2013) further developed and compared four vanadium valence state oxybarometers: (1) spinel-melt; (2) olivine-melt; (3) spinel-olivine; and (4) V/(Cr + Al) in spinel-melt. Papike et al. (2015) illustrated the relationships between the valence state of Cr, V, and Fe and their relationship to spinel stability and composition in martian basalts. Bell et al. (2014) explored by XANES (X-ray Absorption Near-Edge Structure) spectroscopy the Cr valence in olivine and its application to understanding the evolution of fO_2 in planetary basalts.

For pyroxene formed under solar nebular conditions, Simon and Grossman (2004; 2006) and especially Simon et al. (2007) examined the contents and valence states of Ti and V in the Ti-, Al-rich pyroxene in refractory inclusions, termed "fassaite" (Dowty and Clark 1973), providing information on materials formed under the highly reducing conditions of the solar nebula (Grossman 1972; Brearley and Jones 1998).

PYROXENE COMPOSITION AND CRYSTAL CHEMISTRY

Papike (1987) shows that there is a very important difference between augite-fassaite (monoclinic space group C2/c) and pigeonite (monoclinic space group $P2_1/c$) *vs.* orthopyroxene (orthorhombic space group Pbca), which involves the stacking of TOT (tetrahedra-octahedra-tetrahedra) units (Papike et al. 1973). As shown in Figure 3, in orthopyroxene the stacking is +, +, -, -, which produces an orthorhombic structure because the offsets cancel. In monoclinic pyroxenes, the stacking is +, +, +, +, resulting in a monoclinic offset. The M2 site is located between the reversed TOT units and is highly constrained to 6-coordination and thus cannot contain significant Ca, which requires 8-coordination. The charge balance exchange is vacancies in the M1 site for $V^{3+}$and V^{4+}:

$$2\,{}^{VI}Mg^{2+} = {}^{VI}\square + {}^{VI}V^{4+} \text{ or}$$

93 $$3^{VI}Mg^{2+} = {}^{VI}\square + 2^{VI}V^{3+},$$

94 as in olivine (Papike et. al 2005, 2013). For every vacancy, orthopyroxene can accommodate one
95 V^{4+} or two V^{3+}. This is the main reason that V^{3+} is more compatible in the olivine and
96 orthopyroxene structures than V^{4+}.

97 The behavior of multivalent cations (Ti, V, Cr) in pyroxenes has been examined in
98 refractory inclusions in carbonaceous chondrites, in angrite liquids, and in martian liquids,
99 represented by meteorites Yamato 980459 (Y98) and QUE 94201. Figure 4 shows the ranges of
100 pyroxene compositions from these meteorites. The figure illustrates the composition of the
101 quadrilateral (QUAD) component, Al (Al^{IV} + Al^{VI}) contents, and the range in the total "others"
102 (non-QUAD component). The major coupled substitutions for incorporation of "others" are
103 given in Table 1. Papike et al. (2005) reviewed previous work and explained the difference
104 between pyroxene QUAD and "Others" components. Cameron and Papike (1981) explained how
105 to calculate the QUAD and "Others" components. Before one can properly plot the pyroxene
106 QUAD components on the pyroxene quadrilateral, the "Others" component must be removed. If
107 the analyses are superior and the "Others components" have been removed, analyses will not plot
108 above the 50% Wo line (i.e., the top of the quadrilateral). This is because the pyroxene structure
109 is not stable to higher Ca addition once the M2 site is filled with calcium. At higher Ca contents,
110 the pyroxenoid structure becomes stable relative to the pyroxene structure. In Figure 4 we show
111 the compositions of fassaite from refractory inclusions in carbonaceous chondrite Allende,
112 fassaite in angrites, and Y98 and QUE pyroxene plotted on quadrilaterals with "others"
113 component removed. Note that none of the analyses plot above the 50% Wo line. In fassaite from
114 Allende CAIs (Fig. 4a), the QUAD component is mostly diopside and the Al contents are high
115 because of the importance of the Ti-Al substitutions, which characterize the "Others"

116 component. Figure 4b shows that the major compositional variation in the angrite pyroxenes is a
117 Mg-ferrous Fe substitution.
118
119 **FASSAITE IN REFRACTORY INCLUSIONS IN CARBONACEOUS CHONDRITES**
120 Early work by Grossman (1972; 1975) presented strong evidence that Ca-, Al-rich
121 refractory inclusions (CAIs) found in carbonaceous chondrites formed at high temperatures early
122 in solar system history. Decades of subsequent work, including isotopic dating (e.g., Amelin et
123 al. 2002), have shown that they are indeed some of the first solids formed in the solar system.
124 Several papers (Simon et al. 1991; Simon and Grossman 2004; 2006; Simon et al. 2007) have
125 reported details of the compositions, including Ti and V valence systematics, of the pyroxene in
126 refractory inclusions. Here we review some of their findings and contrast pyroxene partitioning
127 behavior between igneous systems (Moon, Mars, and Earth) with the fassaite studies referenced
128 above.
129 **Crystal chemistry**
130 The Ti-rich pyroxene in refractory inclusions was termed "fassaite" by Dowty and Clark
131 (1973). According to Deer et al. (1978), the term was first applied to a pyroxene from an augite
132 syenite limestone in Fassa valley, Trentino, Italy, where it occurs as light- to dark-green crystals
133 in a distinct habit with the zone {110} strongly developed. Subsequently, the name has more
134 generally been used to describe aluminum-rich, Na-poor pyroxenes commonly found in
135 metamorphosed limestones and dolomites, but fassaite has also been reported from eclogitic
136 inclusions in kimberlite, and in meteorites, especially in the CAIs discussed here. The structure
137 of an Al-rich pyroxene that could be termed fassaite, in which ~25% of the tetrahedral sites are
138 occupied by Al, was determined by Peacor (1967). Its unit cell has a = 9.794, b = 8.906, c =

5.319 Å, and a beta angle of 105.9°. It crystallizes in space group C2/c. The crystal structure is essentially that of diopside ($CaMgSi_2O_6$). Ordering of Ca is complete; it fills the M2 site, with 8-fold coordination. The crystal structure of an extremely Ti-, Al-rich fassaite from the Allende meteorite, with a formula of $Ca_{1.00}Mg_{0.39}Ti_{0.48}Al_{0.13}(Al_{0.74}Si_{1.26})O_6$, was determined by Dowty and Clark (1973). Typically, 50-60% of the Ti in meteoritic fassaite is trivalent, and all of the Ti is in the M1 site (Dowty and Clark 1973; Haring et al. 2012), which departs a little more from regularity than in diopside. Fassaite compositions are commonly described as solid solutions of four endmembers: diopside; kushiroite, $CaAl(Al,Si)O_6$; grossmanite, $CaTi^{3+}(Al,Si)O_6$; and a Ti^{4+} component, $CaTi^{4+}Al_2O_6$. Note that all endmembers, and therefore fassaite itself, have one Ca cation per six oxygen anions.

Refractory inclusions: Formation conditions, classification and bulk compositions

The Ti^{3+}/Ti^{4+} ratios of fassaite found in refractory inclusions are evidence of their formation in the solar nebula (Beckett 1986; Grossman et al. 2008). Due to its high proportions of hydrogen and carbon relative to oxygen, the solar nebula was a very reducing environment, with an oxygen fugacity ~7 orders of magnitude below the iron-wüstite buffer (IW-7) (Allende Prieto et al. 2002). In such a gas, at the temperatures of refractory inclusion formation, oxidized iron is not stable and Fe condenses as metal. These conditions are below the Ti_2O_3/TiO_2 buffer, so that both Ti^{3+} and Ti^{4+} can be present, providing an oxybarometer with calibration of this ratio against oxygen fugacity for the phase compositions and equilibria relevant to fassaite-bearing refractory inclusions. This was done in a rigorous set of controlled-atmosphere experiments on refractory inclusion composition analogs (Beckett 1986; Grossman et al. 2008). In Grossman et al. (2008), equilibrium constants were experimentally determined for two reactions and applied

to six natural samples, yielding fO_2s of $10^{-19.9}$ – $10^{-21.2}$ for Type A inclusions and $10^{-18.3}$ – $10^{-19.8}$ for Type B inclusions (at 1500˚C), close to the solar value (Allende Prieto et al. 2002).

Type A inclusions are very melilite-rich, with minor to moderate amounts of spinel, perovskite, and very Ti-rich fassaite. Type B inclusions have much higher fassaite contents (>30 vol.%), moderate melilite and spinel contents, minor anorthite contents, and little or no perovskite (Grossman 1975; 1980). Type C inclusions are relatively rare and have major anorthite contents (30-60 vol.%) and lesser amounts of fassaite, melilite and spinel (Wark 1987; Beckett and Grossman 1988). Modal mineralogical variations are illustrated in Figure 5, which clearly shows how melilite-rich Type A inclusions are, and that they exhibit a much narrower bulk composition range than Type Bs. Stolper (1982) and Stolper and Paque (1986) showed that Type B inclusions crystallized from partially molten assemblages with an equilibrium crystallization sequence of spinel, melilite, anorthite and fassaite. MacPherson et al. (1984) reported, however, that reverse zoning seen in late melilite in some Type B inclusions reflects the appearance of fassaite before anorthite at cooling rates between 0.5 and 50°C/hour. The Type B inclusions are subdivided into two textural subtypes (Wark and Lovering 1977): B1s, with thick, nearly monomineralic melilite mantles enclosing fassaite-, spinel-, anorthite-rich cores; and B2s, which have no melilite mantles, a relatively uniform distribution of phases and rather typical-looking igneous textures.

Type B2 inclusions tend to have higher SiO_2 contents, and therefore higher fassaite/melilite ratios, than Type B1s, as seen in Figure 5. Using the method of Stolper (1982), Simon and Grossman (2006) projected bulk compositions of Type B inclusions onto the gehlenite-forsterite-anorthite plane of the CaO-MgO-Al_2O_3-SiO_2 (CMAS) system and found a continuum of compositions, from B1s that project near the center of the spinel+melilite field, to

184 the most SiO_2-rich B2, that projects onto the join between the spinel+melilite field and the
185 spinel+anorthite field.

186 **Fassaite compositions**

187 Fassaite in Type A inclusions tends to be more Ti-rich than that in Type Bs and not
188 strongly zoned. Cores of normally-zoned fassaite grains in Type B inclusions are Ti-, V-, and Sc-
189 rich and Si-, Mg-poor compared to their rims. Those in B1s tend to have stronger concentric
190 zoning, with higher core Ti contents than those in Type B2 inclusions. Sector-zoned grains are
191 more common in Type B2 inclusions than in B1s (Simon and Grossman 2006). There is a strong
192 correlation between MgO and SiO_2 contents, which can be thought of as reflecting the diopside
193 component of the fassaite composition, and this is illustrated in Figure 6a. The complementary
194 anticorrelation between MgO and total Ti is shown in Figure 6b. Total Al contents are only
195 weakly correlated with total Ti contents (Fig. 6c). This is because Al enters both M1 and
196 tetrahedral sites, and as Ti contents increase, the Al contents of the tetrahedral sites increase, but
197 the proportions of Al in octahedral (M1) coordination decrease, as shown in Figure 6d.
198 Tetrahedral Al contents are highest, and octahedral Al contents lowest, in the Ti-rich fassaite of
199 Type A inclusions.

200 It has also been shown (Simon et al. 1991) that Ti^{3+} is more strongly compatible than Ti^{4+}
201 in fassaite; those workers derived crystal/liquid distribution coefficients of ~2.7 for Ti^{3+} and ~0.7
202 for Ti^{4+}. In addition, Simon et al. (1991) found that, in fassaite in Type B1 inclusions (those with
203 thick melilite mantles enclosing pyroxene-rich cores), Ti^{3+}/Ti^{4+} ratios decrease from crystal cores
204 to rims. This indicates that the melt from which they grew became depleted in Ti^{3+}, which also
205 means that it was isolated from the nebular gas; otherwise the melt would have maintained redox
206 equilibrium with the ambient gas and its Ti^{3+}/Ti^{4+} ratio would have remained constant, as appears

to have been the case in Type B2 inclusions. Simon and Grossman (2006) showed that, while total Ti contents decrease from core to rim in fassaite grains in Type B2 inclusions (pyroxene-rich with no melilite mantle), the Ti^{3+}/Ti^{4+} ratios in them do not decrease from core to rim.

Another interesting and important observation is that BSE images and electron probe analyses show that sudden increases, or "spikes", in Ti and V contents and in Ti^{3+}/Ti^{4+} ratios (Fig. 7) are commonly observed in the outer margins of large fassaite grains in Type B1 inclusions (Simon et al. 1992; Simon and Grossman 2006), but such variations do not occur in the abundances of other compatible (e.g., Sc) or incompatible (e.g. rare earth) elements. Noting that the spikes could not be attributed to incoming of a late phase and that the elements that show sharp increases are multivalent under nominal nebular redox conditions, Simon et al. (2007) conducted XANES analytical traverses to assess the changes in valence across the spikes. The XANES data confirmed the change in Ti valence but simultaneous changes in V valence were not observed. The preferred explanation for the observations is that in Type B1 inclusions, the late liquid from which the fassaite crystallized was isolated from the reducing nebular gas by the melilite mantle. Because of its higher compatibility in fassaite, Ti^{3+} was drawn down in the melt relative to Ti^{4+} during the fassaite-dominated stage of crystallization. Near the end of crystallization, nebular gas leaked in, reducing the Ti and V, making them more compatible. The valence of V was then modified by an electron exchange reaction with Ti. Because Type B2 inclusions do not have melilite mantles, their melts were able to maintain communication with the nebular gas, and as a result their grains are not zoned with respect to Ti^{3+}/Ti^{4+} ratios and do not exhibit late "spikes" in Ti and V contents.

BSE, Ti, Al, Mg mapping of zoned fassaite

Elemental X-ray maps of the area that includes the location of the traverse plotted in Figure 7 are shown in Figure 8. Vanadium was difficult to map because of Ti-V interferences, especially Ti K_β on V K_α. The pronounced spike illustrated in Figure 7 resulted from a major reducing event in the inclusion, resulting in an increase in Ti^{3+}/Ti^{4+}. The reducing event is not only recorded by Ti^{3+}, which is inferred from electron probe analyses but requires XANES techniques to directly measure, but also by Al, which enters pyroxene with Ti in an important coupled substitution. This is reflected in Al concentrations, which are easily measured with the electron microprobe, and the maps in Figure 8 show this clearly, with Al following Ti. Because the M2 site in fassaite is filled with Ca, the charge balance equation takes on a simple form, namely:

$$\text{Excesses: } {}^{VI}Al^{3+} + {}^{VI}Sc^{3+} + {}^{VI}Cr^{3+} + {}^{VI}V^{3+} + {}^{VI}Ti^{3+} + 2\,{}^{VI}Ti^{4+} = \text{Deficiencies: } {}^{IV}Al^{3+},$$

(coefficients indicate the magnitude of the excess/deficiency, such that $^{VI}Al^{3+}$ is equivalent to 1 charge excess, while $2\,^{VI}Ti^{4+}$ indicates that for every Ti^{4+} substitution, there is a charge excess of 2). By far the most important charge balance couples are $^{VI}Ti^{3+}$ - $^{IV}Al^{3+}$ and $^{VI}Ti^{4+}$- 2 $^{IV}Al^{3+}$. Within the main zoning trend from the large Ti spike to the crystal boundary, the pyroxene "others" components (Papike et. al 2005) decrease while Mg increases in the M1 site to take their place.

VARIATION IN THE VALENCE STATES OF V AND Cr IN ANGRITE MELTS

Angrites exhibit a range in mineralogy, textures, and isotopic systematics, implying derivation through a range of thermal and crystallization histories from plutonic to volcanic (e.g. Baker et al. 2005; Amelin et al. 2011; Keil 2012). They represent some of the earliest stages of planetesimal differentiation (e.g. Mittlefehldt et al. 1998; Baker et al. 2005; Amelin 2008; Kaltenbach et al. 2011; Amelin et al. 2011; Brennecka and Wadhwa 2012; Keil 2012). Not

surprisingly, there is no simple petrogenetic model for their origin. Mittlefehldt et al. (2002) concluded, "There is no simple petrogenetic sequence, partial melting with or without fractional crystallization that has been proposed to explain the suite of angrites." Jambon et al. (2005) reached a similar conclusion, writing "no simple conventional model is expected to provide a suitable solution to their petrogenesis." Although these conclusions underscore the difficulty in interpreting the origin of angrites, numerous studies (e.g. Floss et al. 2003; Jambon et al. 2005; McKay et al. 1995; McKay and Wagstaff 1991; Mittlefehldt et al. 1998, 2002) have identified potential processes that contributed to their generation. Although impact and nebular condensate origins have been proposed, many other observations suggest an igneous origin (e.g. McCoy et al. 2003, 2006a,b; Keil 2012). For example, Jurewicz and McKay (1993), Jurewicz et al. (1995), and Mittlefehldt et al. (2002) demonstrated that melting of chondritic material (e.g. CM, CV) under redox conditions where iron metal is unstable (e.g. IW+1 to IW+2) produced angrite-like melts. Alternatively, Kurat et al. (2004), Jambon et al. (2005), and Mikouchi et al. (2015) suggested that angrites were produced under more reducing conditions (<IW) with their exotic melt compositions resulting from carbonates in the source.

Clearly, understanding what role fO_2 played in the production of angrite magmas is critical for deciphering their petrogenesis and extending our understanding of primordial melting of asteroids. Calculations for the fO_2 conditions of angrite production/crystallization are limited and only preliminary attempts been made to understand the changes in fO_2 during petrogenesis. Many of the angrites have phase assemblages which provide conflicting signals about redox conditions during crystallization (e.g. Fe metal and a Fe-Ti oxide with potential Fe^{3+}, i.e., McKay 1989; Mikouchi et al. 2011; Keil 2012). There have been several estimates of fO_2 for angrites (Brett et al. 1977; McKay 1989; Mikouchi et al. 2008; King et al. 2012) based on valence state

partitioning in pyroxene. The pyroxene in angrites is aluminum-titanium diopside (i.e., fassaite), strongly zoned in Fe-Mg (Mg# ranges from 74 to 0), with nearly constant and high Ca (Wo component >50%) (Mittlefehldt et al. 1998). The Al and Ti contents of these fassaites are much lower than those of the Ti-rich pyroxene in refractory inclusions. Pyroxene in many angrites has complicated zoning with respect to Al_2O_3 and TiO_2 contents. For example, in Asuka 881371, both Al_2O_3 and TiO_2 are high in magnesium-rich crystal cores and initially drop with decreasing Mg#. At lower Mg# values, Al_2O_3 contents become constant or increase slightly, whereas TiO_2 contents continue to decrease. Experiments by Crozaz and McKay (1990) investigated experimentally the variation of D_{Eu}/D_{Gd} with fO_2, between plagioclase and pyroxene in equilibrium with an angrite melt composition. This ratio reflects the valence state partitioning behavior of Eu^{2+} and Eu^{3+} with changing fO_2. Crozaz and McKay (1990) estimated the fO_2 of crystallization to be approximately IW+0.6 for angrite LEW 86010. This estimate is a "snapshot" of fO_2 conditions during co-crystallization of plagioclase and pyroxene. More germane to the topic of the present paper are the XANES analyses of V redox state in pyroxenes from D'Orbigny reported by King et al. (2012). They observed changes in the valence state of V from 2.91 for the earliest pyroxenes to 3.1 for the late-stage pyroxenes that occur in the mesostasis and extend into voids. Assuming limited temperature and compositional effects, these changes in V valence state translate to changes in fO_2 from IW-0.7 during early pyroxene crystallization to IW+0.5 during later episodes of pyroxene crystallization. As this was a preliminary report, it presented limited information concerning the effects of pyroxene orientation and composition on the V valence measurements. Further investigations of Cr and V valence state behavior in angrites as a function of fO_2 would allow testing of models for primordial melting of chondritic material to produce the angrite parent melts, examining the influence of fO_2 on angrite

298 petrogenesis, as well as assessing angrite melt evolution. The latter is of particular interest, as a
299 recent study of Asuka 881371 indicates that its xenocrysts (i.e. olivine) may represent fragments
300 of the angrite parent body mantle (Mikouchi et al. 2015).
301
302 **MARTIAN MELTS**
303 **Cr partitioning between pigeonite-melt and augite-melt**
304 Several recent studies have demonstrated that Cr^{3+}/Cr^{total} in basaltic melts changes
305 dramatically as fO_2 increases from values near the IW buffer to values near the FMQ buffer
306 (Hanson and Jones 1998; Berry et al., 2006; Bell et al., 2014). In order to graphically
307 demonstrate the effects of increasing fO_2 on the Cr^{3+}/Cr^{total} in the melt, we have modeled the
308 melt's Cr^{3+}/Cr^{total} based on XANES measurements, at several different crystallization
309 temperatures (Fig. 9). The curves were modeled using equilibrium constants for the Cr^{3+}-Cr^{2+}
310 equilibrium from the crystallization experiments presented in Bell et al. (2014 and 2015). The
311 equilibrium constants used in the modeling were derived from XANES measurements of the Cr
312 valence ratio of quenched experimental melts equilibrated under reduced conditions (i.e., IW-1)
313 to ensure that the presence of Fe^{3+} did not modify the Cr valence ratio. In addition to the intrinsic
314 temperature effects, the model curves also contain the effects of changing melt composition, as
315 the composition of the experimental melts evolved with continued crystallization. The data from
316 these experiments were then used in the following equation to model the Cr valence ratios (from
317 Bell et al. 2014):

$$\frac{Cr^{2+}}{\Sigma Cr} = \left[1 + e^{\left(\frac{1}{4} ln fO_2 + lnK'\right)}\right]^{-1}$$

318 While not explicitly stated in the equation, temperature has a significant effect on the equilibrium
319 Cr valence ratio of the melt, because decreasing temperature stabilizes Cr^{3+} relative to Cr^{2+}. It is

important to note that the composition of the Y98 experimental liquids also varied with temperature, therefore, the observed effects of decreasing temperature are not only caused by the intrinsic effects of temperature on the Cr valence equilibrium, but perhaps also by changes in melt composition due to increasing degree of crystallization. There are variations in the slopes of the model curves (Fig. 9) because the availability of Cr^{3+} in the melt is controlled by a combination of fO_2, temperature, and melt composition.

Karner et al. (2007b) addressed the valence state partitioning of Cr between pyroxene and melt in a martian basalt composition based on meteorite QUE 94201. Karner et al. (2007a) used the partitioning of Cr and V between pyroxene and melt to estimate the oxygen fugacity conditions for martian basalt QUE 94201 crystallization. This was possible because both Cr and V are multivalent elements and their partitioning behavior between pyroxene and melt (D values) is primarily determined by fO_2. The approach was to produce experimental charges of QUE 94201 composition at IW-1, IW, and IW+1, allowing for pyroxene crystallization exclusively. The charges were then used to calibrate D_{Cr} and D_V oxybarometer curves based on the partitioning between early-crystallizing pyroxene (pigeonite cores) and the bulk starting composition. Martian basalt QUE 94201 represents a liquid composition (McKay et al. 2003), so using D_{Cr} and D_V pigeonite/melt in both the synthetic charges and natural samples was the best way to estimate fO_2 at the beginning of crystallization. Application of the calibrated oxybarometers to QUE 94201 yielded fO_2 estimates of IW+0.2 and IW+0.9, based on D_{Cr} and D_V, respectively (McKay et al. 2003). These estimates were considered credible by Karner et al. (2007a; b) for several reasons, but it is now apparent that Cr and V partitioning into pyroxene is not controlled by oxygen fugacity alone (see Figures 10, 11 and 12 and discussion of charge balance couples below). Karner et al. (2007b) explore in detail how the availability of Al and Na

for coupled substitution affects D_{Cr} between pigeonite/melt and augite/melt in synthetic QUE 94201 composition samples. That early study presented XANES data on the valence state of Cr in both the glass and pyroxene phases. Cr partitioning data for augite and pigeonite as a function of fO_2 and $Na+{}^{IV}Al$ are illustrated in Figures 10a and 10b, respectively. These plots show that Ds for pigeonite are lower than those for augite and that they increase with increasing fO_2. Direct Cr valence measurements by XANES in pyroxene (Fig. 11), however, do not show any systematic trend as a function of fO_2 from IW-1 to IW+1. This may indicate the importance of coupled substitutions on Cr partitioning into pyroxene.

Crystal chemical basis for Vanadium partitioning behavior in pyroxene

Early work on V partitioning was reported by Canil (e.g. Canil 1999, 2002), who was one of the first to report that V^{3+} is more compatible than V^{4+} in pyroxene. Experiments on the QUE 94201 composition (Karner et al. 2008) show that D_V augite/melt is greater than D_V pigeonite/melt in samples equilibrated under the same fO_2 conditions (Fig. 12). This increase is due to the increased availability of elements for coupled substitution with the V^{3+} or V^{4+} ions, namely Al and Na, in augite compared to pigeonite. Therefore, more V can enter into the augite structure, as per:

$$^{IV}Al^{3+}_{x} + {}^{VIII}Na^{+}_{1-x} = {}^{VI}V^{3+} \text{ or}$$

$$^{IV}Al^{3+}_{x} + {}^{VIII}Na^{+}_{2-x} = {}^{VI}V^{4+}$$

To investigate the degree to which valence influences partitioning behavior, XANES can be used to make a direct determination of V valence in a given phase. Sutton et al. (2005) established the foundation for this technique when they examined the valence of V in volcanic and impact glasses from the Earth, Moon, and Mars. Karner et al. (2006) demonstrated that the

365 fO_2 conditions determined for these volcanic glasses and glass beads were consistent with those
366 calculated using other oxybarometers.

367 The advantage of measuring V valence in glasses is that, unlike those for minerals, the
368 XANES spectra of glasses are not complicated by orientation effects (see Dyar et al. 2002;
369 McCanta et al. 2004). Such orientation effects are a result of the synchrotron radiation
370 preferentially sampling the crystal structure in the polarization plane (typically horizontal).
371 Measurements of iron valence in pyroxene show that orientation effects result in an uncertainty
372 of ±20% in Fe^{3+}/Fe total (McCanta et al. 2004). For V in olivine and pyroxene, these orientation
373 effects are of similar magnitude (Sutton et al. 2002; Sutton and Newville 2005).

374 Karner et al. (2008) applied the technique developed by Sutton et al. (2005) to the QUE
375 94201-composition run products. Figure 13 shows the results of XANES measurements of the
376 valence state of V in pyroxene, olivine, and co-existing glass from that study. The glass data
377 show a steady increase in V valence from mostly V^{3+} at IW-1 to mostly V^{4+} at IW+3.5, which is
378 consistent with our assessment that V^{3+} and V^{4+} are the dominant valences of V in basaltic melts
379 over this range of fO_2 values. There is evidence for non-negligible V^{2+} in the glass at IW-1, but
380 this valence determination is almost within error of 3. Turning to the mineral data, pyroxene
381 formed at IW-1 to IW+1 contains mostly V^{3+}. These measurements confirm the idea that V^{3+} is
382 more compatible in pyroxene than V^{4+}, which accounts for the decrease in D_V with increasing
383 fO_2 seen in augite and in pigeonite. As Figure 12 shows, for example, augite and pigeonite
384 formed at IW+1 have lower D_Vs, despite having higher $Na+^{IV}Al$, than augite and pigeonite
385 formed at IW-1, because of the lower V^{3+}/V^{4+} in the melt at higher fO_2. Finally, Karner et al.
386 (2008; Fig. 13) determined that the valence state of V in olivine crystallized at QFM is
387 approximately 70% V^{3+}.

By comparing the glass data to the mineral data (Fig. 13) we can make several observations about the valence state partitioning of V into olivine and pyroxene. First, the difference in V valence between olivine (mostly 3+) and co-existing glass (mostly 4+) seen at IW+3.5 suggests that V^{3+} is more compatible than V^{4+} in the olivine structure. This observation is consistent with conclusions drawn from previous partitioning studies (Papike et al. 2005; Shearer et al., 2006). Second, the pyroxene-melt relationship at IW+1 is similar to that for olivine-melt at IW+3.5 in that pyroxene also favors V^{3+} over V^{4+}. At IW+1, the glass is about 80% V^{3+} and 20% V^{4+}, but the pyroxene shows only V^{3+}. Again, the difference between the glass and pyroxene shows that V^{3+} is more compatible in pyroxene than V^{4+}, as indicated by previous partitioning studies (Canil 1999; Toplis and Corgne 2002; Papike et al. 2005). This is not surprising, as V^{3+} is a better fit in the M1 site and creates a smaller charge excess than V^{4+}. This also results in simpler substitution mechanisms for V^{3+} into the pyroxene structure. The data at IW show that all the V in both the glass and pyroxene is V^{3+} (within error), and thus there is no difference in V valence between the two phases. The data show that both the glass and pyroxene at IW-1 may contain a small percentage of V^{2+}, and again, there is essentially no difference in V valence between the glass and pyroxene at this low fO_2.

The compatibility of both V^{3+} and V^{4+} in the pyroxene structure is ultimately dependent on the Ca concentration. The orthopyroxene structure (Fig. 3a) cannot contain significant Ca, which requires 8-coordination. This favors smaller cations over V^{3+} and V^{4+}, which have larger radii than the nominal cations, Mg^{2+} and Fe^{2+} (Fig. 2). That is why orthopyroxene has much lower D_V than clinopyroxene (Fig. 14).

THE RELATIVE IMPORTANCE OF COUPLED SUBSTITUTION IN PYROXENE FROM DIFFERERENT PLANETARY RESERVOIRS

Papike et al. (2005) laid the foundation for consideration of valence state partitioning of Cr, Fe, Ti, Al, and V among crystallographic sites in olivine, pyroxene, and spinel from planetary basalts. That paper illustrated the plethora of possible coupled substitution mechanisms in pyroxene (Table 1) using the following equation:

Excesses: $^{VI}Al^{3+} + {}^{VI}Fe^{3+} + {}^{VI}Cr^{3+} + {}^{VI}V^{3+} + {}^{VI}Ti^{3+} + 2\,{}^{VI}Ti^{4+} + {}^{VI}2V^{4+} =$

Deficiencies: $^{IV}Al^{3+} + {}^{M2}Na^{+}$.

These authors showed the importance of cation size and also charge balance in substitution mechanisms. Figure 14 shows the importance of the effect of wollastonite (Wo) content on the V Ds for pyroxene, with olivine for comparison. Karner et al. (2008) address the substitution of V into the pyroxene structure. Coupled substitutions are required for incorporation of V^{3+} and V^{4+} into the pyroxene crystal structure because these cations replace divalent Mg and Fe in the M1 site (Papike et al. 2005), thus creating charge excesses of +1 or +2, respectively. Crystal charge balance must be maintained and can be accomplished by simultaneously substituting 1) an Al cation(s) into the tetrahedral site for Si or 2) a Na cation(s) into the M2 site for Ca. An increase in D_V from pigeonite to augite can be explained by the ease with which Al and/or Na, if available, can enter augite (compared to pigeonite) and the availability of that charge couple in the melt. Table 1 shows the relative importance of various coupled substitutions in four environments: Solar Nebula, Moon, Mars, and Earth, based on correlations observed in analyses.

PYROXENE AS A RECORDER OF PLANETARY PARENTAGE AND PROCESSES

Pyroxene is a very powerful recorder of planetary processes and parentage. Often, analyses of a single grain (with some combination of the analytical tools, electron microprobe, SIMS, and XANES) from a planetary sample can yield key information about the oxygen fugacity during formation and aspects of the parental melts. Papike (1996) discusses pyroxene as a recorder of cumulate formational processes in asteroids, Moon, Mars, and Earth. The author points out that from REE contents of orthopyroxene cores determined by SIMS and knowledge of the OPX/melt partition coefficients, the REE contents of the parental melts can be estimated. Papike et al. (2003) discuss the determination of planetary parentage using only the microprobe by using Mn/Fe ratios in all pyroxene structure types. The most complete data set for using this technique is found in Papike et al. (2009), who showed that the Mn/Fe ratios of pyroxene increase in the order Moon, Earth, Mars, and 4 Vesta. Another strong clue to planetary parentage is the types of coupled substitution that are found in pyroxene (note Table 1). The techniques of microXANES and electron microprobe analysis can be also be used to identify the source of a grain and can, for example, even distinguish between fassaite from a Type B1 and fassaite from a Type B2 inclusion (Simon and Grossman 2006). Even without access to XANES techniques, ratios of $^{IV}Al/^{VI}Al$ can be used as a proxy for Ti valence in these Al-, Ti-rich pyroxenes.

IMPLICATIONS AND FUTURE WORK

In mineralogy, petrology, and cosmochemistry, there are "superminerals." Pyroxene is one such mineral. To be a "supermineral," the mineral phase must occur in diverse igneous and gas reservoirs and record the intensive thermodynamic parameters, processes, and planetary parentage and conditions in planetary bodies and the solar nebula. In addition, the phase must be able to accommodate a broad range of the periodic table of elements and display diverse crystal

455 structures. Pyroxene meets these metrics. In this paper, we have reviewed some of the ways
456 pyroxene has already been used to serve as a petrologic and geochemical recorder. However, as
457 powerful as pyroxene is already, it can be made more effective if some of the following
458 objectives are met. With respect to chromium, vanadium, and titanium: 1) we must conduct more
459 experiments on diverse bulk compositions over larger ranges of oxygen fugacity, temperature,
460 and pressures; 2) we must obtain a more robust XANES calibration and further develop data
461 reduction techniques; 3) we must try to improve the spatial resolution of all of our analytical
462 techniques; and 4) we must be able to investigate intracrystalline valance state partitioning
463 among various crystallographic sites.
464

465 **ACKNOWLEDGEMENTS**

466 This research was funded by a NASA Cosmochemistry grant NNX13AH85G to C.
467 Shearer and the Institute of Meteoritics. S. Simon was supported by NASA grant NNX13AE73G
468 (L. Grossman, PI).
469

470 **REFERENCES CITED**

471 Allende Prieto, C., Lambert D.L., and Asplund M. (2002) A reappraisal of the solar photospheric
472 C/O ratio. Astrophys. J. Lett. 573, L137-L140.
473
474 Amelin, Y. (2008) U-Pb ages of angrites. Geochimica et Cosmochimica Acta 72, 221–232.
475
476 Amelin, Y., Krot, A.N., Hutcheon, I.D., and Ulyanov A.A. (2002) Lead isotopic ages of
477 chondrules and calcium-aluminum-rich inclusions. Science 297, 1679-1683.

Amelin, Y., Kaltenbach, A. and Stirling, C.H. (2011) The U-Pb systematics and cooling rate of plutonic angrite NWA 4590. 42nd Lunar and Planetary Science Conference, Abstract #1682. Lunar and Planetary Institute, Houston.

Baker, J., Bizzarro, M., Wittig, N., Connelly, J. and Haack, H. (2005) Early planetesimal melting from an age of 4.5662 Gyr for differentiated meteorites. Nature 436, 1127-1131.

Beckett, J.R. (1986) The origin of calcium-, aluminum-rich inclusions from carbonaceous chondrites: An experimental study. Ph.D. dissertation, The University of Chicago.

Beckett, J.R. and Grossman, L. (1988) The origin of type C inclusions from carbonaceous chondrites. Earth & Planetary Science Letters, 89, 1-14.

Bell, A.S., Burger, P.V., Le, L., Shearer, C.K., Papike, J.J., Sutton, S.R., Newville, M., and Jones, J. (2014) XANES measurements of Cr valence in olivine and their application to planetary basalts. American Mineralogist, 99, 1404-1412.

Bell, A.S., Burger, P.V., Shearer, C.K., and Papike, J.J. (2015) Decoding the redox history recorded in the olivine megacrysts of Yamato 980459 with chromium K-edge XANES. 46th Lunar and Planetary Science Conference, Abstract #2421, Lunar and Planetary Institute, Houston.

501 Berry, A.J., O'Neill, H. St. C., Scott, D.R., Foran, G.J., and Shelly, J.M.G. (2006) The effect of
502 composition of Cr^{2+}/Cr^{3+} in silicate melts. American Mineralogist, 91, 1901-1908.
503
504 Brearley, A.J. and Jones, R.H. (1998) Chondritic meteorites. In J. Papike, Ed., Planetary
505 Materials, p. 3-1 – 3-398. Reviews in Mineralogy, 36, Mineralogical Society of
506 American, Washington, D. C.
507
508 Brennecka, G.A., and Wadhwa, M., (2012) Uranium isotope compositions of the basaltic angrite
509 meteorites and the chronological implications for the early Solar System. Proceedings of
510 the National Academy of Sciences 109, 9299-9303.
511
512 Brett, R., Huebner, J.S., and Sato, M. (1977) Measured oxygen fugacities of the Angra dos Reis
513 achondrite as a function of temperature. Earth & Planetary Science Letters 35, 363–368.
514
515 Cameron, M., and Papike, J.J. (1981) Structural and chemical variation in pyroxenes. American
516 Mineralogist, 66, 1-50.
517
518 Canil, D. (1999) Vanadium partitioning between orthopyroxene, spinel, and silicate melt and the
519 redox states of mantle source regions for primary magmas. Geochimica et Cosmochimica
520 Acta, 63, 557-572.
521
522 Canil, D. (2002) Vanadium in peridotites, mantle redox states and tectonic environments:
523 Archean to present. Earth & Planetary Science Letters, 195,75-90.

Crozaz, G., and McKay, G. (1990) Rare earth elements in Angra dos Reis and Lewis Cliff 86010, two meteorites with similar but distinct magma evolutions. Earth & Planetary Science Letters 97, 369–381.

Deer, W.A., Howie, R.A., and Zussman, J. (1978) Rock Forming Minerals, Volume 2a, Single-chain silicates. 668 pp. John Wiley & Sons, New York.

Dowty, E., and Clark, J.R. (1973) Crystal structure refinement and optical properties of a Ti^{3+} fassaite from the Allende meteorite. American Mineralogist, 58, 230-242.

Dyar, M.D., Gunter, M.E., Delaney, J.S., Lanzarotti, A., and Sutton, S.R. (2002) Systematics in the structure, optical properties, and XANES spectra of pyroxenes, amphiboles, and micas. Canadian Mineralogist 40, 1375-1393.

Floss, C., Crozaz, G., McKay, G., Mikouchi, T., and Killgore, M. (2003) Petrogenesis of angrites. Geochimica et Cosmochimica Acta 67, 4775–4789.

Grossman, L. (1972) Condensation in the primitive solar nebula. Geochimica et Cosmochimica Acta, 36, 597-619.

Grossman, L. (1975) Petrography and mineral chemistry of Ca-rich inclusions in the Allende meteorite. Geochimica et Cosmochimica Acta, 39, 433-454.

Grossman, L. (1980) Refractory inclusions in the Allende meteorite. Annual Review of Earth and Planetary Sciences 8, 559-608.

Grossman, L., Beckett, J.R., Fedkin, A.V., Simon, S.B., and Ciesla, F.J. (2008) Redox conditions in the solar nebula: Observational, experimental, and theoretical constraints. In MacPherson et al. (Eds.), Oxygen in the Solar System, Reviews in Mineralogy and Geochemistry 68, 93-140.

Hanson, B. and Jones, J. (1998) The systematics of Cr^{3+} and Cr^{2+} partitioning between olivine and liquid in the presence of spinel. American Mineralogist, 83, 669-684.

Haring, M.M., Flemming R.L., Terskikh, V., Grossman, L. and Simon, S.B. (2012) Crystal structure and cation ordering in fassaite from Type B CAI TS62B in Allende CV3. 43rd Lunar and Planetary Science Conference, Abstract #2601, Lunar and Planetary Institute, Houston.

Jambon, A., Barrat, J.A., Boudouma, O., Fonteilles, M., Badia, D., Gopel, C., and Bohn, M. (2005) Mineralogy and petrology of the angrite Northwest Africa 1296. Meteoritics & Planetary Science 40, 361–375.

568 Jurewicz, A.J.G. and McKay, G.A. (1993) Angrite LEW87051: Are the olivines pheno's or
569 xeno's? A continuing story (abstract). Lunar and Planetary Science Conference XXIV,
570 737–738. Lunar and Planetary Institute, Houston.
571
572 Jurewicz, A.J.G., Mittlefehldt, D.W., and Jones, J.H. (1995) Experimental partial melting of the
573 St Severin (LL) and Lost City (H) chondrites. Geochimica et Cosmochimica Acta 59,
574 391–408.
575
576 Kaltenbach, A., Stirling, C.H., and Amelin, Y. (2011) Revised ages of angrites. Mineralogical
577 Magazine 75, 1137.
578
579 Karner, J.M., Sutton, S.R., Papike, J.J., Shearer, C.K., Jones, J.H., and Newville, M. (2006)
580 Application of a new vanadium valence oxybarometer to basaltic glasses from Earth,
581 Moon, and Mars. American Mineralogist, 91, 270-277.
582
583 Karner, J.M., Papike, J.J., Shearer, C.K., McKay, G., Le, L. and Burger, P. (2007a) Valence
584 state partitioning of Cr and V between pyroxene-melt: Estimates of oxygen fugacity for
585 martian basalt QUE 94201. American Mineralogist, 92, 1238-1241.
586
587 Karner, J.M., Papike, J.J., Sutton, S.R., Shearer, C.K., McKay, G., Le, L., and Burger, P. (2007b)
588 Valence state partitioning of Cr between pyroxene-melt: Effects of pyroxene and melt
589 composition and direct determination of Cr valence by XANES. Application to martian
590 basalt QUE 94201 composition. American Mineralogist, 92, 2002-2005.

Karner, J.M., Papike, J.J., Sutton, S.R., Shearer, C.K., Burger, P.V., McKay, G. and Le L. (2008) Valence state partitioning of V between pyroxene-melt: Effects of pyroxene and melt composition and direct determination of V valence states by XANES. Application to martian basalt QUE 94201 composition. Meteoritics & Planetary Science, 43, 1275-1285.

Keil, K. (2012) Angrites, a small but diverse suite of ancient, silica-undersaturated volcanic-plutonic mafic meteorites, and the history of their parent asteroid. Chemie der Erde 72, 191-218.

King, P.L., Sutton, S.R., Spilde, M.N., Wirick, S., Lanzirotti, A., and Agee, C.B. (2012) Redox history of early solar system planetesimals recorded in the D'Orbigny angrite. 43rd Lunar and Planetary Science Conference, Abstract #2436. Lunar and Planetary Institute, Houston.

Kurat, G., Varela, M.E., Brandstätter, F., Weckwerth, G., Clayton, R.N., Weber, H.W., Schultz, L., Wäsch, E., and Nazarov, M.A. (2004). D'Orbigny: a non-igneous angritic achondrite. Geochimica et Cosmochimica Acta 68, 1901–1924.

MacPherson, G.J., Paque, J.M., Stolper, E.M. and Grossman, L. (1984) The origin and significance of reverse zoning in melilite from Allende Type B inclusions. Journal of Geology 92, 289-305.

McCanta, M.C., Dyar, M.D., Rutherford, M.J., and Delaney, J.S. (2004) Iron partitioning between basaltic melts and clinopyroxene as a function of oxygen fugacity. American Mineralogist, 89, 1685-1693.

McCoy, T.J., Wilson, L., Benedix, G.K., and Ketcham, R.A. (2003) Vesicles in meteorites: the angle on angrites (Abstract). Meteoritics & Planetary Science 38 (Suppl), A65.

McCoy, T.J., Ketcham, R.A., Wilson, L., Benedix, G.K., Wadhwa, M., and Davis, A.M., (2006a) Formation of vesicles in asteroidal basaltic meteorites. Earth & Planetary Science Letters 246, 102–108.

McCoy, T.J., Mittlefehldt, D.W., and Wilson, L. (2006b) Asteroid differentiation. In: Meteorites and the Early Solar System II. (eds. D.S Lauretta and H.Y McSween Jr.) University of Arizona Press, Tucson, 733–745.

McKay, G.A. (1989) Partitioning of rare earth elements between major silicate minerals and basaltic melts. In: Reviews in Mineralogy 21 (eds. B.R. Lipin and G.A. McKay) 45-77.

McKay, G. and Wagstaff, J. (1991) Olivines in angrite LEW 87051: Phenos or xenos? Meteoritics (Abstract) 26, 370.

McKay, G., Crozaz, G., Mikouchi, T. and Miyamoto, M. (1995) Exotic olivine in Antarctic angrites Lewis Cliff 87051 and Asuka-881371. Meteoritics (Abstract) 30, 543–544.

McKay, G., Le, L., Koizumi, E. and Mikouchi, T. (2003) Additional constraints on the crystallization of basaltic shergottite QUE 94201. 34th Lunar and Planetary Science Conference, Abstract #2109. Lunar and Planetary Institute, Houston.

Mikouchi, T., McKay, G., and Jones, J. (2008) Petrogenesis and crystallization history of quenched angrites (abstract). Meteoritics & Planetary Science, 43, A98.

Mikouchi, T., McKay, G.A., Miyamoto, M., and Sugiyama, K. (2011) Olivine xenocrysts in quenched angrites: The first "differentiated" materials in the Solar System? (Abstract). Workshop on the Formation of the First Solids in the Solar System, Kauai, HI, November 7–9.

Mikouchi, T., Hasegawa, H., Takenouchi, A., and Kagi, H. (2015) Olivine xenocrysts in Asuka 881371 angrite revisited. 46th Lunar and Planetary Science Conference, Abstract #2065. Lunar and Planetary Institute, Houston.

Mittlefehldt , D.W., McCoy, T.J., Goodrich, C.A., and Kracher, A. (1998) Non-chondritic meteorites from asteroidal bodies. In J.J. Papike, Ed., Planetary Materials, 36, p. 4-1 – 4-195. Reviews in Mineralogy, Mineralogical Society of America, Chantilly, VA.

658 Mittlefehldt, D.W., Kilgore, M., and Lee, M.T. (2002) Petrology and geochemistry of
659 D'Orbigny, geochemistry of Sahara 99555, and the origin of angrites. Meteoritics &
660 Planetary Science 37, 345–369.
661
662 Papike, J.J. (1987) Chemistry of the rock-forming silicates: Ortho, ring, and single-chain
663 structures. Reviews of Geophysics, 25, 1483-1526.
664
665 Papike, J.J. (1996) Pyroxene as a recorder of cumulate formational processes in Asteroids,
666 Moon, Mars, Earth: Reading the record with the ion microprobe. "Mineralogical Society
667 of America Presidential Address." American Mineralogist, 81, 525-544.
668
669 Papike, J.J., Prewitt, C.T., Sueno, S., and Cameron, M. (1973) Pyroxenes: Comparisons of real
670 and ideal structural topologies. Zeitschrift für Kristallographie, 138, 254-273.
671
672 Papike, J.J., Karner, J.M., and Shearer, C.K. (2003) Determination of planetary basalt parentage:
673 A simple technique using the electron microprobe. American Mineralogist, 88, 469-472.
674
675 Papike, J.J., Karner, J.M., and Shearer, C.K. (2004) Comparative planetary mineralogy: V/(Cr
676 +Al) systematics in chromite as an indicator of relative oxygen fugacity. American
677 Mineralogist 89, 1557-1560.
678

679 Papike, J.J., Karner, J.M., and Shearer, C.K. (2005) Comparative planetary mineralogy: Valence
680 state partitioning of Cr, Fe, Ti, and V among crystallographic sites in olivine, pyroxene,
681 and spinel from planetary basalts. American Mineralogist, 90, 277-290.
682
683 Papike, J.J., Karner, J.M., Shearer, C.K., and Burger, P.V. (2009) Silicate Mineralogy of Martian
684 Meteorites. "Invited Review" Geochimica et Cosmochimica Acta, 73, 7443-7485.
685
686 Papike, J.J., Karner, J.M., Shearer, C.K. and Burger, P.V. (2010) Valence state partitioning of V
687 between augite/melt crystallized from a highly spiked martian basalt composition as a
688 function of oxygen fugacity (IW-1 to FMQ). 41st Lunar and Planetary Sciences
689 Conference, Abstract #1010. Lunar and Planetary Institute, Houston.
690
691 Papike, J.J., Burger, P.V., Bell, A.S., Le, L., Shearer, C.K., Sutton, S.R., Jones, J. and Newville
692 M. (2013) Developing vanadium valence state oxybarometers (spinel-melt, olivine-melt,
693 spinel-olivine) and V/(Cr + Al) partitioning (spinel-melt) for martian olivine-phyric
694 basalts. American Mineralogist, 98, 2193-2196.
695
696 Papike, J.J., Burger, P.V., Bell, A.S., Shearer, C.K., Le, L., Jones, J., and Provencio, P. (2014)
697 Valence state partitioning of V between pyroxene and melt for martian melt compositions
698 Y980459 and QUE94201: The effect of pyroxene composition and crystal structure.
699 American Mineralogist, 99, 1175-1178.
700

Papike, J.J., Burger, P.V., Bell, A.S., Shearer, C.K., Le, L. and Jones, J. (2015) Normal to inverse transition in spinel: Understanding the interplay of chromium, vanadium, and iron valence state partitioning through a crystal chemical lens. American Mineralogist, invited "Outlook Paper" for the American Mineralogist Centennial, in press.

Peacor, D.R. (1967) Refinement of the crystal structures of a pyroxene of formula $M_IM_{II}(Si_{1.5}Al_{0.5})O_6$. American Mineralogist, 52, 31-41.

Shannon, R.D., and Prewitt, C.T. (1969) Effective ionic radii in oxides and fluorides. Acta Crystal, B25, 925-946.

Shearer, C.K., McKay, G., Papike, J.J., and Karner, J.M. (2006) Valence state partitioning of vanadium between olivine-liquid: Estimates of oxygen fugacity of Y980459 and application to other olivine-phyric martian basalts. American Mineralogist, 91, 1657-1663.

Simon, S.B., and Grossman, L. (2004) A preferred method for the determination of bulk compositions of coarse-grained refractory inclusions and some implications of the results. Geochimica et Cosmochimica Acta, 68, 4237-4248.

Simon, S.B., and Grossman, L. (2006) A comparative study of melilite and fassaite in types B1 and B2 refractory inclusions. Geochimica et Cosmochimica Acta, 70, 780-798.

724 Simon, S.B., Grossman, L. and Davis, A.M. (1991) Fassaite composition trends during
725 crystallization of Allende Type B refractory inclusion melts. Geochimica et
726 Cosmochimica Acta, 55, 2635-2655.
727
728 Simon, S.B., Davis, A.M. and Grossman, L. (1992) Evidence for changes in redox state during
729 crystallization of Allende type B1 inclusions (abstract). Meteoritics 27, 289-290.
730
731 Simon, S.B., Sutton, S.R., and Grossman, L. (2007) Valence of titanium and vanadium in
732 pyroxene in refractory inclusion interior and rims. Geochimica et Cosmochimica Acta,
733 71, 3098-3118.
734
735 Stolper E. (1982) Crystallization sequences of Ca-Al-rich inclusions from Allende: An
736 experimental study. Geochimica et Cosmochimica Acta, 46, 2159-2180.
737
738 Stolper, E. and Paque, J.M. (1986) Crystallization sequences of Ca-Al-rich inclusions from
739 Allende: The effects of cooling rate and maximum temperature. Geochimica et
740 Cosmochimica Acta, 50, 1785-1806.
741
742 Sutton, S.R. and Newville, M. (2005) Vanadium K XANES of synthetic olivine: Valence
743 determinations and orientation effects. 36th Lunar and Planetary Science Conference,
744 Abstract #2133. Lunar and Planetary Institute, Houston.
745

Sutton, S.R., Simon, S., Grossman, L., Delaney, J.S., Beckett, J., Newville, M., Eng, P., and Rivers, M. (2002) Evidence for divalent vanadium in Allende CAI fassaite and implications for formation conditions. 33rd Lunar and Planetary Science Conference, Abstract #1907. Lunar and Planetary Institute, Houston.

Sutton, S.R., Karner, J., Papike, J., Delaney, J.S., Shearer, C., Newville, M., Eng, P., Rivers, M., and Dyar, M.D. (2005) Vanadium K edge XANES of synthetic and natural basaltic glasses and application to microscale oxygen barometry. Geochimica et Cosmochimica Acta, 69, 2333-2348.

Toplis, M.J. and Corgne, A. (2002) An experimental study of element partitioning between magnetite, clinopyroxene and iron-bearing silicate liquids with particular emphasis on vanadium. Contributions to Mineralogy and Petrology, 144, 22-37.

Wark, D.A. (1987) Plagioclase-rich inclusions in carbonaceous meteorites: liquid condensates? Geochimica et Cosmochimica Acta, 51, 221-242.

Wark, D.A. and Lovering, J.F. (1977) Marker events in the early evolution of the solar system: Evidence from rims on Ca-Al-rich inclusions in carbonaceous chondrites. Proc. Lunar Sci. Conf. 8th, 95-112.

FIGURE CAPTIONS

Figure 1. Valences of some of the most important multivalent cations in igneous systems and condensates in the solar system and the oxygen fugacity ranges over which they are dominant. The individual points represent oxygen fugacity conditions where the proportions of two valence states are approximately equal. Colored arrows represent the three elements discussed here: green for chromium, blue for vanadium, and red for titanium. IW: Iron-Wüstite; QFM: Quartz-Fayalite-Magnetite. After Figure 1 in Papike et al. (2005).

Figure 2. Ionic radii (nm) of octahedrally coordinated cations discussed in this paper. Note that Cr^{3+}, V^{3+}, Fe^{3+}, and Ti^{3+} cluster closely over a small range. The cations in red are the most compatible in the pyroxene M1 site. After Figure 2 in Papike et al. (2005), based on data from Shannon and Prewitt (1969).

Figure 3. (a) The crystal structure of orthopyroxene, space group Pbca. The M2 site (6-coordinated) contains a small amount of Ca (~2-4% Wo) and is illustrated with green spheres. This site takes cations in order of preference, Ca^{2+}, Mn^{2+}, Fe^{2+}, and Mg^{2+}. The M1 site (illustrated with red spheres) takes Al^{3+}, Cr^{3+}, V^{3+}, Fe^{3+}, and Ti^{3+} cations (listed in order of increasing ionic radius) in addition to divalent cations. The stacking of the TOT (tetrahedral-octrahedral, tetrahedral units is + + - -. (b) The crystal structure of pigeonite, space group P21/c, portrayed as a projection down the *b*-axis to illustrate the TOT stacking sequence of + + + + that leads to a monoclinic unit cell. (c) The crystal structure of orthopyroxene projected down the *c*-axis to eliminate overlap of the M2 sites (green) and M1 sites (red). (d) The crystal structure of C2/c augite showing the chains of orange M1 octahedra and M2 sites with 8 coordinating oxygens, as well as chains of corner-sharing tetrahedra (yellow). The plane of projection (b-c

plane) is likely the best-fit boundary (or "optimal phase boundary") between orthopyroxene and pigeonite.

Figure 4. Wo-En-Fs quadrilaterals for naturally occurring pyroxenes discussed in this manuscript: (a) CAIs, (b) angrites, (c) Y98, and (d) QUE 94201. Pyroxene crystallization trajectories are indicated by arrows. Area of each symbol represents the extent of Al substitution into the pyroxene. Approximate range of "Others" components in each pyroxene population is presented under each quadrilateral plot.

Figure 5. Ternary diagram showing the mineralogical proportions in Types A, B, and C refractory inclusions in terms of melilite, fassaite, and other components. A representative field for Type B inclusions is illustrated in blue; individual points represent modal analyses of Types B1 and B2. Modified from Figure 2 in Wark (1987).

Figure 6. Comparison of compositions of fassaite from Types A and B coarse-grained refractory inclusions. Fassaite in Type A inclusions is richer in Ti and poorer in Mg and Si than that in Type B inclusions. (a) MgO vs. SiO_2. (b) MgO vs. TiO_2^{tot} (all Ti treated as TiO_2). (c) Al_2O_3 vs. TiO_2^{tot}. (d). Proportions of Al cations in tetrahedral and octahedral sites as a function of Ti cations per six oxygen anions. There is much overlap between Type A and Type B fassaite in total Al contents but a clear difference in the distribution of Al between the crystallographic sites.

Figure 7. Results from an electron probe traverse across a "spike" near the edge of a fassaite grain in Allende Type B1 inclusion TS34. (a) Abundances of Al^{3+} and Ti^{3+} cations in the M1 site. (b) The corresponding variation of $Ti^{3+}/(Ti^{3+} + Ti^{4+})$. Error bars have been omitted for clarity; typical uncertainties on the $Ti^{3+}/(Ti^{3+} + Ti^{4+})$ ratio are on the order of ±0.05.

Figure 8. Four electron microprobe maps, with the location and direction of the traverse illustrated in Figure 7 shown by the arrow. (a) BSE map. (b) Al WDS map. (c) Mg WDS map. (d) Ti WDS map. Note that Al is a good proxy for Ti. Warmer colors (e.g. red, orange) indicate higher X-ray intensities, and cooler colors (e.g. blue, green) lower intensities, with white being the highest, black the lowest.

Figure 9. Modeled Cr^{3+}/ total Cr in QUE 94201 melts as a function of fO_2 (modified from Figure 2b in Papike et al. 2015).

Figure 10. (a) D_{Cr} for augite/melt and pigeonite/melt *vs.* fO_2 for synthetic pyroxenes crystallized from a melt of QUE 94201 composition. Also shown are the equation and the R^2 value for each best-fit line. Error bars (x-axis) for each data point are based on the fO_2 calibration of furnaces at the Johnson Space Center laboratory, while the y-axis errors are smaller than the size of the symbols, representing the uncertainty associated with the standard deviation of several Cr electron microprobe measurements in determining *D*-values. After Figure 2a in Karner et al. (2007b). (b) D_{Cr} for pigeonite/melt and augite/melt *vs.* Na + ^{IV}Al atoms per formula unit (afu) in the respective pyroxene. Tie-lines connect pigeonite and augite from the same sample and the stated fO_2. After Figure 2b in Karner et al. (2007b).

836

837 Figure 11. Cr valence state as determined by XANES for pigeonite and co-existing glass at IW-
838 1, IW, and IW+1 for experimental charges using the QUE 94201 composition. Also shown are
839 the data for olivine and co-existing glass for a sample produced at IW+3.5 (QFM). After Figure 3
840 in Karner et al. (2007b).

841

842 Figure 12. D_V for pigeonite/melt and augite/melt versus Na + ^{IV}Al atoms per formula unit (apfu)
843 in the respective pyroxene in QUE 94201-composition melts. Tie-lines connect pigeonite and
844 augite from the same sample and the fO_2 is indicated. After Figure 5 in Karner et al. (2008).

845

846 Figure 13. V valence state as determined by XANES for pigeonite and co-existing glass at IW-1,
847 IW, and IW+1 in experimental charges. Also shown are the data for olivine and co-existing
848 glass for the sample produced at IW+3.5 (QFM). After Figure 6 in Karner et al. (2008).

849

850 Figure 14. Ds for V in pyroxene/glass for compositions QUE 94201 and Y98. Results are shown
851 for augite (QUE 94201 composition with wollastonite [Wo]=33 mol.%), pigeonite (QUE 94201
852 composition with Wo=13 mol.%, and orthopyroxene (Y98 composition with Wo<4 mol.%).
853 Olivine is also shown for comparison. In all cases, the error bars represent the 1σ propagated
854 error. The REE-doped samples are spiked with 0.1 wt.% V_2O_3 and 0.6 wt. % of 9 REE each.
855 Modified after Figure 1a in Papike et al. (2014).

Table 1. Fe, Cr, V and Ti valence state variation with $fO2$. The second part of the table shows the major coupled substitutions into the pyroxene structure.*

Solar Nebula: IW-7	Moon: IW-2 to IW-1	Mars: IW to IW+4	Earth: IW+2 to IW+6
Multivalent elements in Condensate and CAIs	**Multivalent elements in basaltic melts**		
$Fe\text{-}Fe^{2+}$	No Fe^{3+}	Fe^{3+} moderate	Fe^{3+} high
Cr^{2+}, Cr^{3+}	Cr^{3+} moderate, Cr^{2+} high	Cr^{3+} high, Cr^{2+} low	mostly Cr^{3+}, Cr^{2+} very low
V^{2+}, V^{3+}	$V^{3+} > V^{4+}$, low V^{2+}	$V^{4+} \approx V^{3+}$	$V^{4+} > V^{3+}$, V^{5+}
Ti^{3+}, Ti^{4+}	Ti^{4+}, Ti^{3+} low	all Ti^{4+}	all Ti^{4+}
Pyroxene charge balance couples = "others"			
none	none	$^{VI}Fe^{3+}\text{-}^{IV}Al$	$^{VI}Fe^{3+}\text{-}^{IV}Al$
none	none	$^{M2}Na - ^{M1}Fe^{3+}$	$^{M2}Na - ^{M1}Fe^{3+}$
none	$^{M1}Cr^{3+}\text{-}^{IV}Al$	$^{M1}Cr^{3+}\text{-}^{IV}Al$	$^{M1}Cr^{3+}\text{-}^{IV}Al$
none	none	$^{M2}Na - ^{M1}Cr^{3+}$	$^{M2}Na - ^{M1}Cr^{3+}$
low	Cr^{2+} for Mg or Fe^{2+}	low	none
none	none	$^{M2}Na^{M1}V^{4+\,IV}Al$	$^{M2}Na^{M1}V^{4+\,IV}Al$
low	low	$^{M1}V^{4+}\text{-}2^{IV}Al$	$^{M1}V^{4+}\text{-}2^{IV}Al$
none	none	$^{M2}Na - ^{M1}V^{3+}$	low
low	$^{M1}V^{3+}\text{-}^{IV}Al$	low	none
low	V^{2+} for Ca, Mg, Fe^{2+}	none	none
high ($^{M1}Ti^{3+}\text{-}^{IV}Al$)	$^{M1}Ti^{3+}\text{-}^{IV}Al$	none	none
high ($^{M1}Ti^{4+}\text{-}2^{IV}Al$)	$^{M1}Ti^{4+}\text{-}2^{IV}Al$	$^{M1}Ti^{4+}\text{-}2^{IV}Al$	$^{M1}Ti^{4+}\text{-}2^{IV}Al$

*Modified from Table 6 in Papike et al. (2005)

Figure 1.

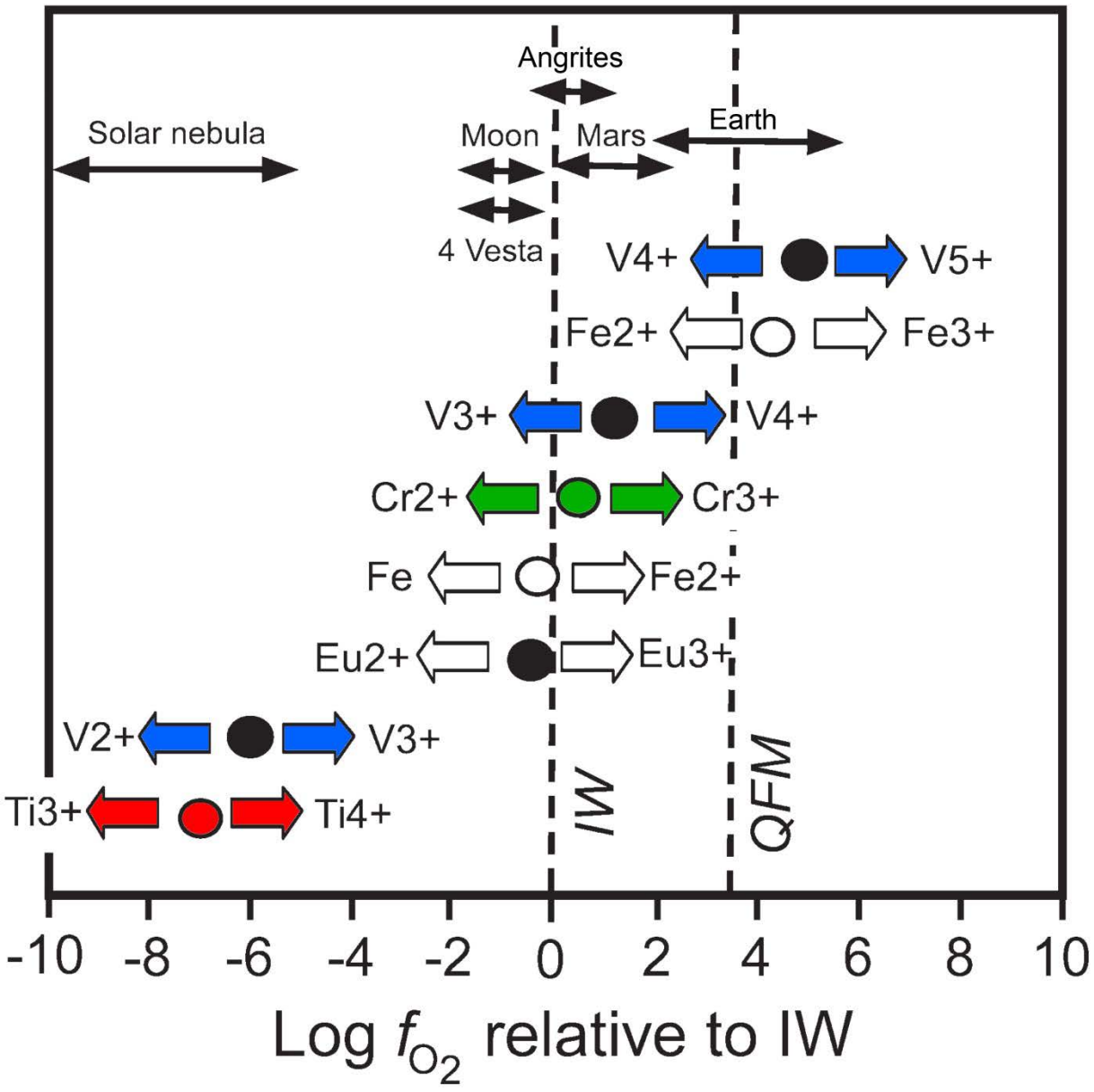
Angrites
Solar nebula
Moon
Mars
Earth
4 Vesta
V4+
V5+
Fe2+
Fe3+
V3+
V4+
Cr2+
Cr3+
Fe
Fe2+
Eu2+
Eu3+
V2+
V3+
Ti3+
Ti4+
IW
QFM
-10
-8
-6
-4
-2
0
2
4
6
8
10
Log f_{O_2} relative to IW

Figure 2.

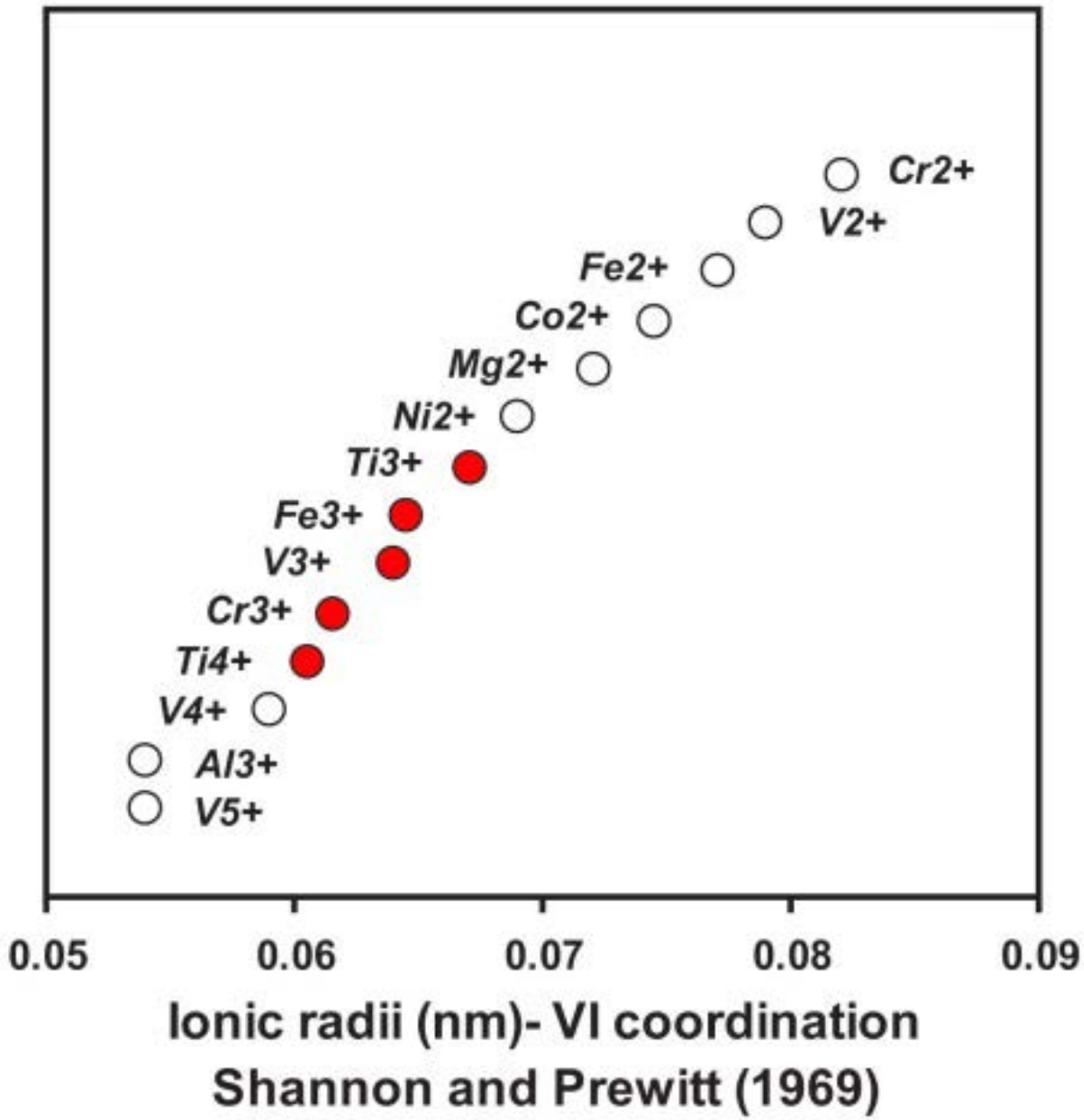
Cr2+
V2+
Fe2+
Co2+
Mg2+
Ni2+
Ti3+
Fe3+
V3+
Cr3+
Ti4+
V4+
Al3+
V5+
0.05
0.06
0.07
0.08
0.09
Ionic radii (nm)- VI coordination
Shannon and Prewitt (1969)

Figure 3.

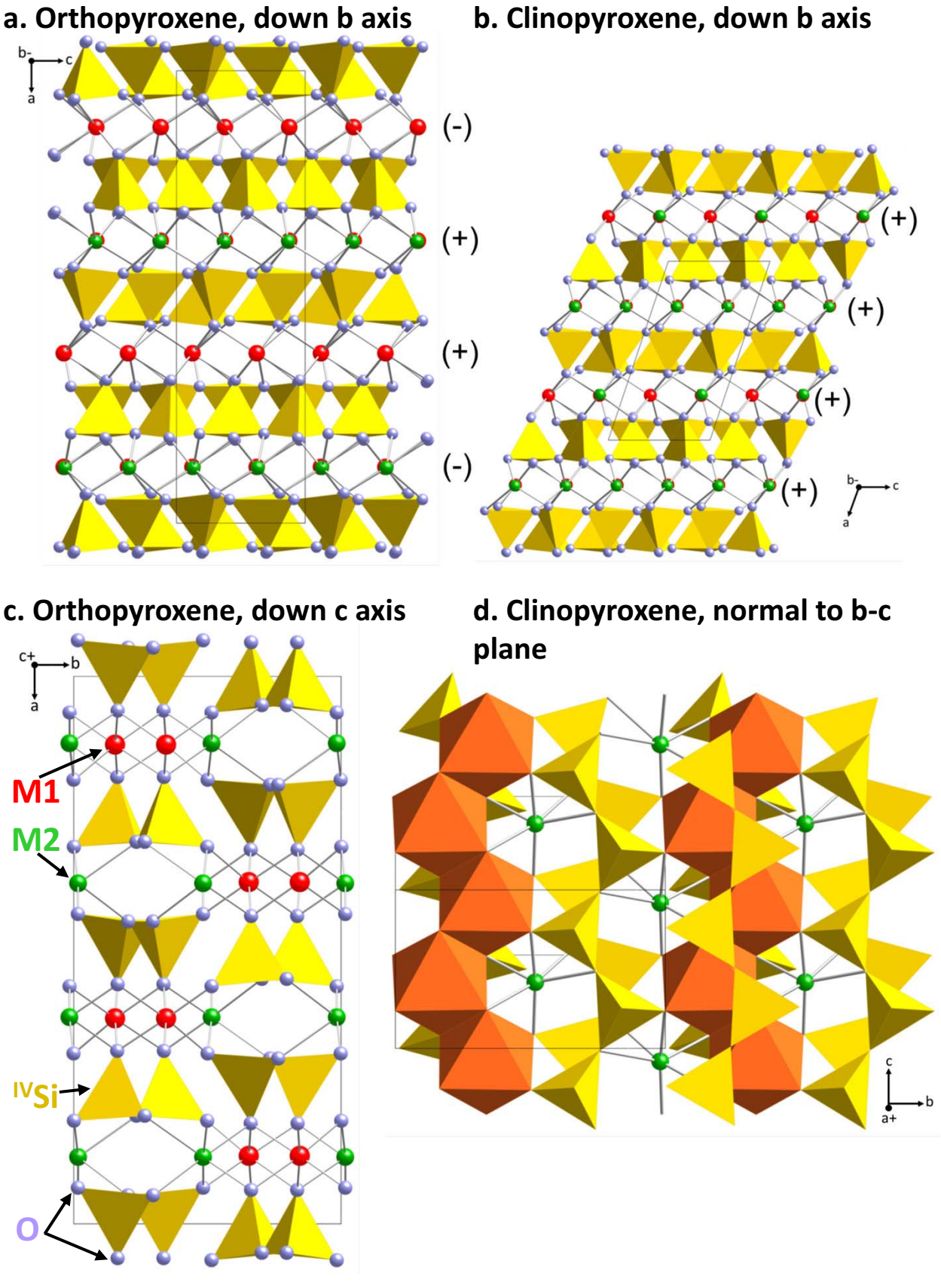
a. Orthopyroxene, down b axis
b-
c
a
(-)
(+)
(+)
(-)
b. Clinopyroxene, down b axis
(+)
(+)
(+)
(+)
b-
c
a
c. Orthopyroxene, down c axis
c+
b
a
M1
M2
IVSi
O
d. Clinopyroxene, normal to b-c plane
c
b
a+

Figure 4.

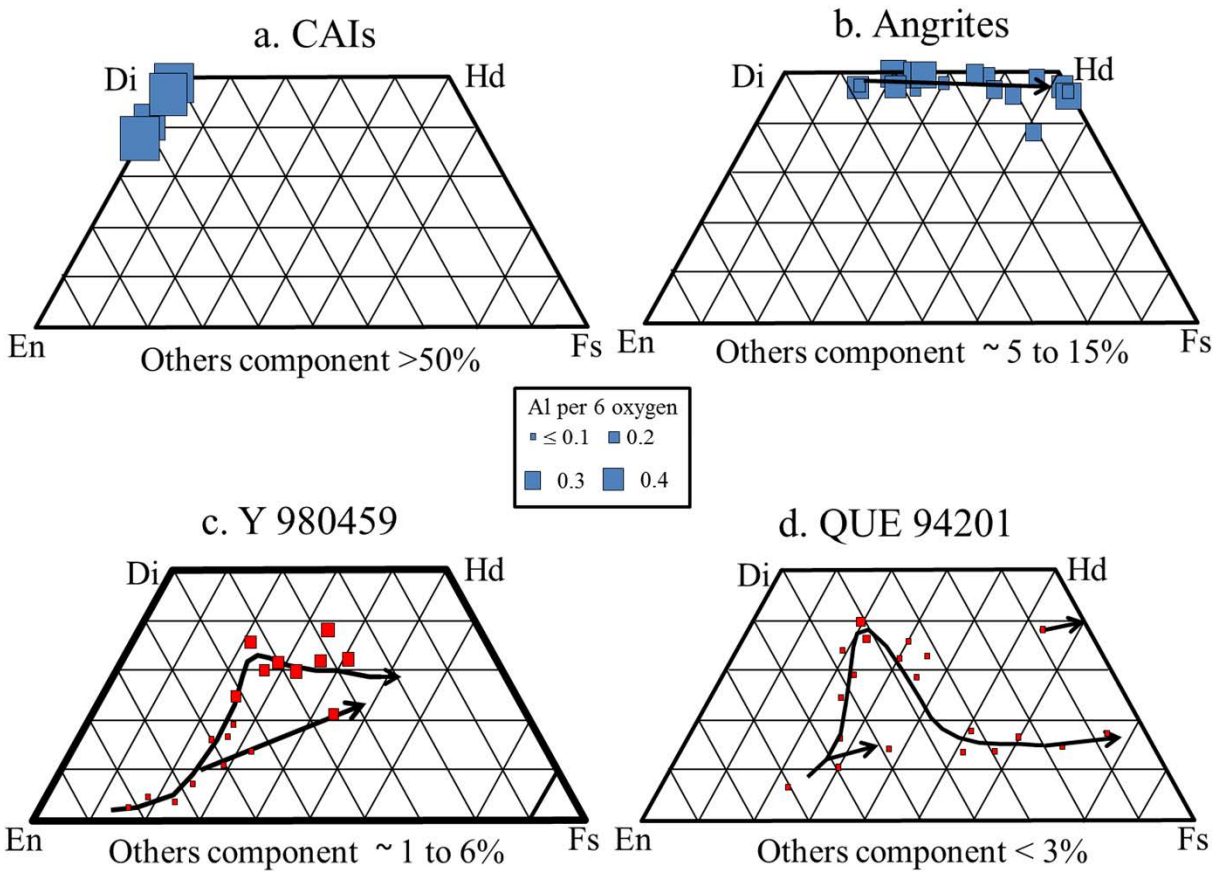
a. CAIs
Di
Hd
En
Fs
Others component >50%
b. Angrites
Di
Hd
En
Fs
Others component ~ 5 to 15%
Al per 6 oxygen
≤ 0.1
0.2
0.3
0.4
c. Y 980459
Di
Hd
En
Fs
Others component ~ 1 to 6%
d. QUE 94201
Di
Hd
En
Fs
Others component < 3%

Figure 5.

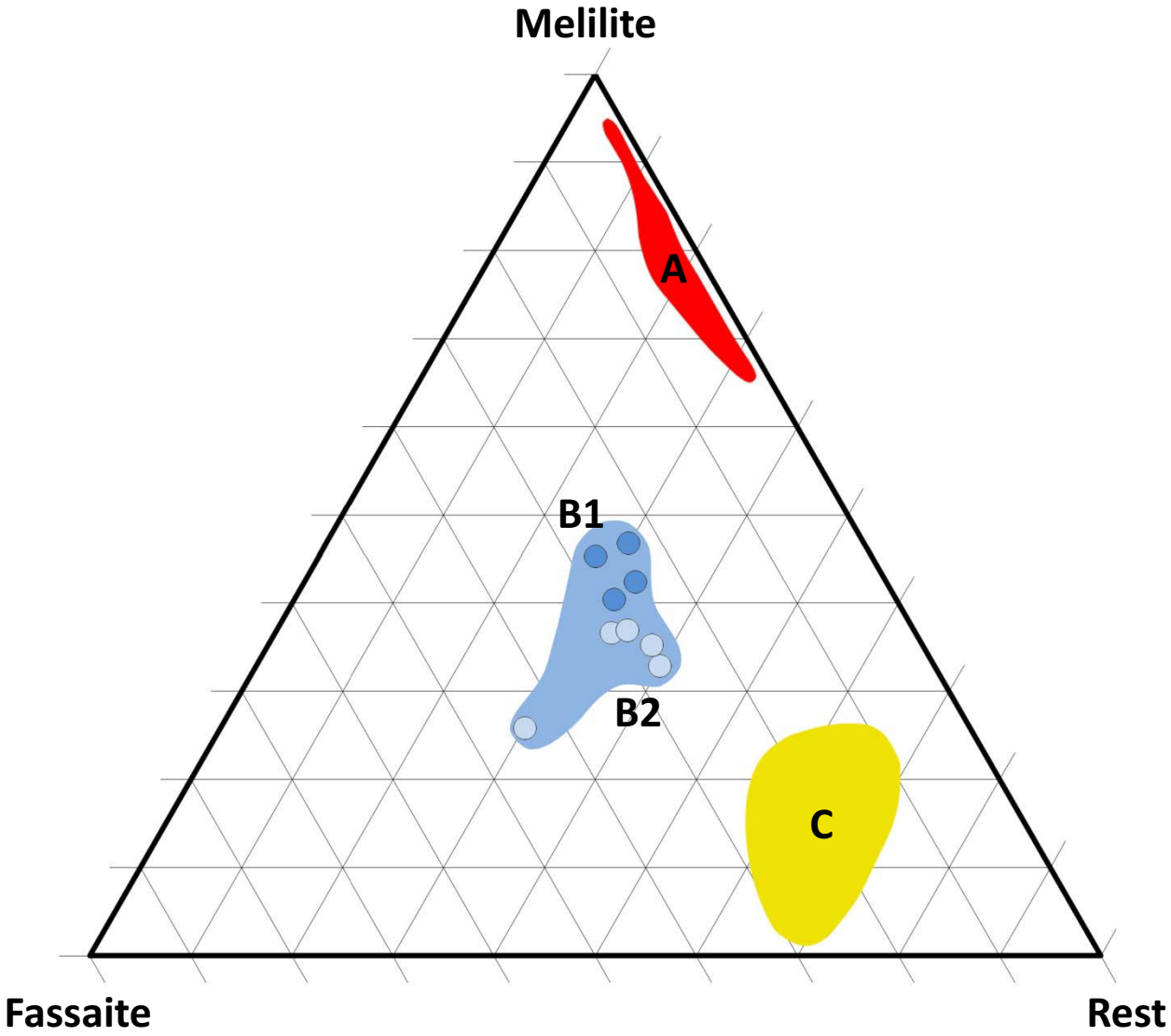

Figure 6.

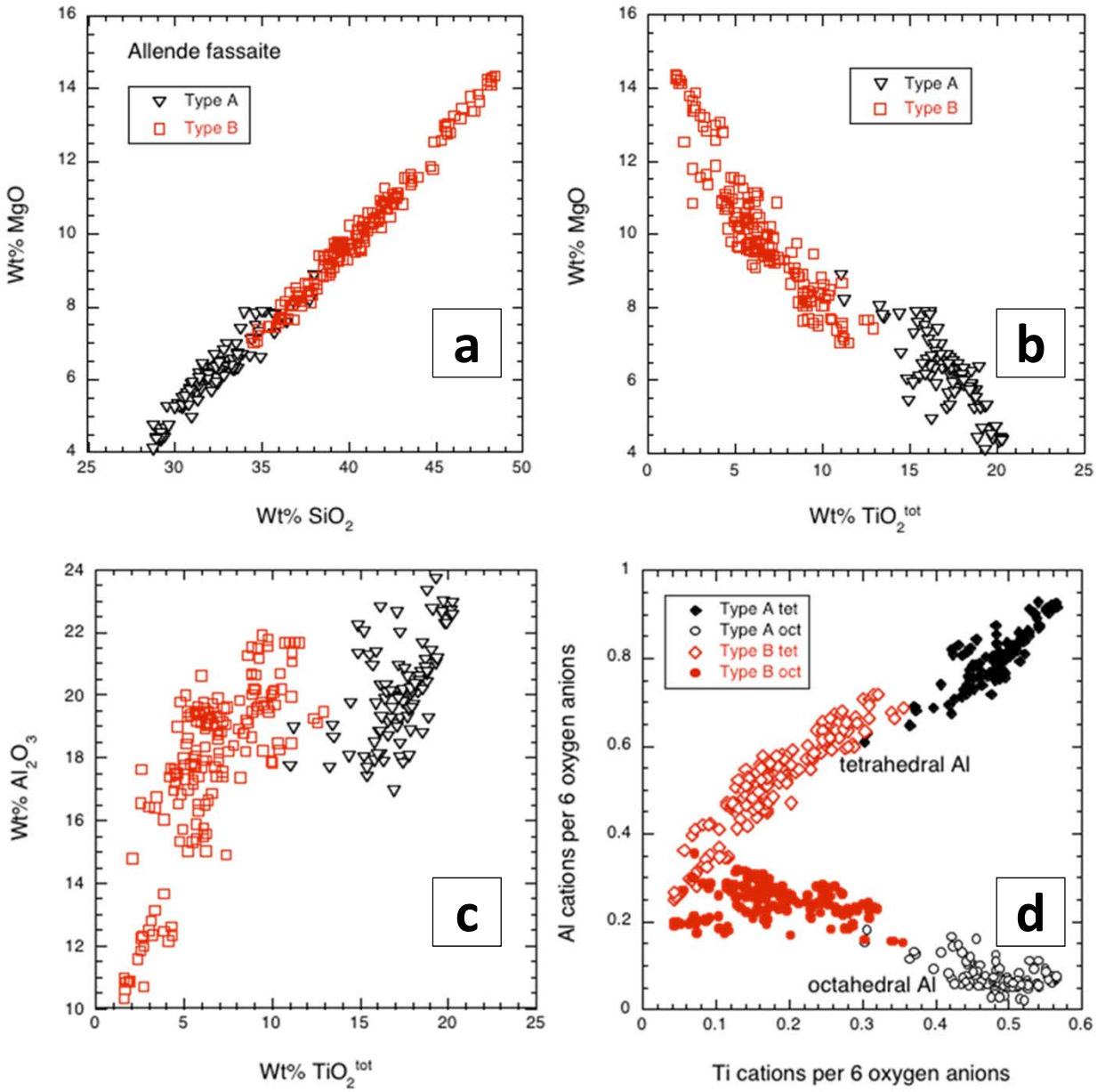
Allende fassaite
Type A
Type B
Wt% MgO
Wt% SiO2
a
Type A
Type B
Wt% MgO
Wt% TiO2 tot
b
Wt% Al2O3
Wt% TiO2 tot
c
Type A tet
Type A oct
Type B tet
Type B oct
tetrahedral Al
octahedral Al
Al cations per 6 oxygen anions
Ti cations per 6 oxygen anions
d

Figure 7.

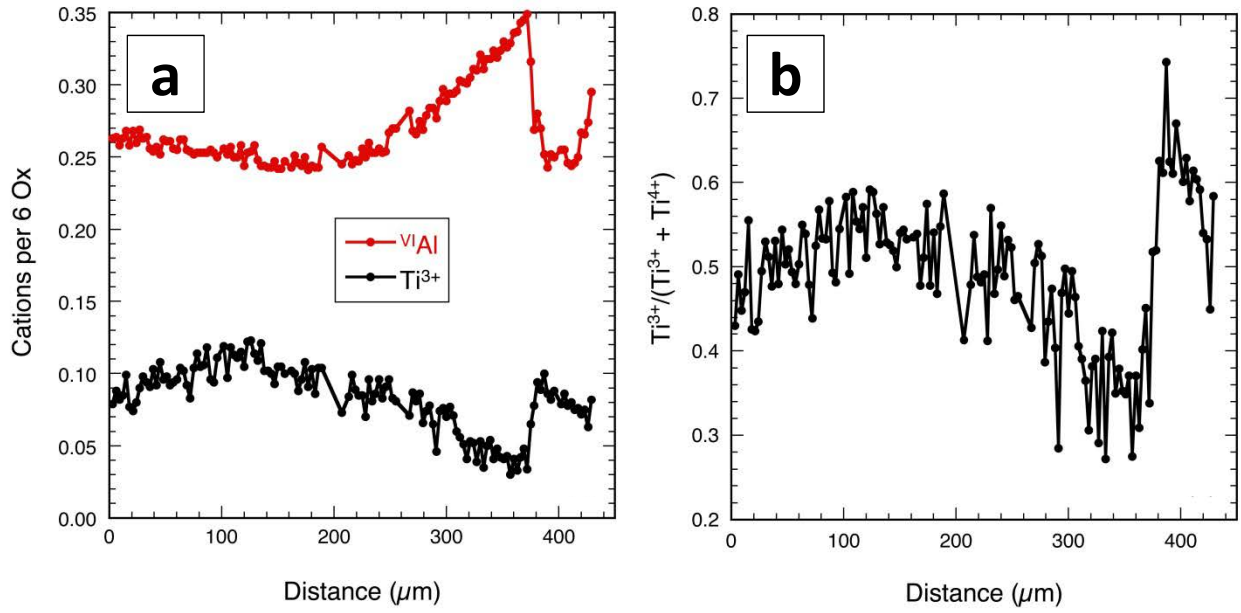
a
b
Cations per 6 Ox
^{VI}Al
Ti^{3+}
$Ti^{3+}/(Ti^{3+} + Ti^{4+})$
Distance (μm)
Distance (μm)

Figure 8.

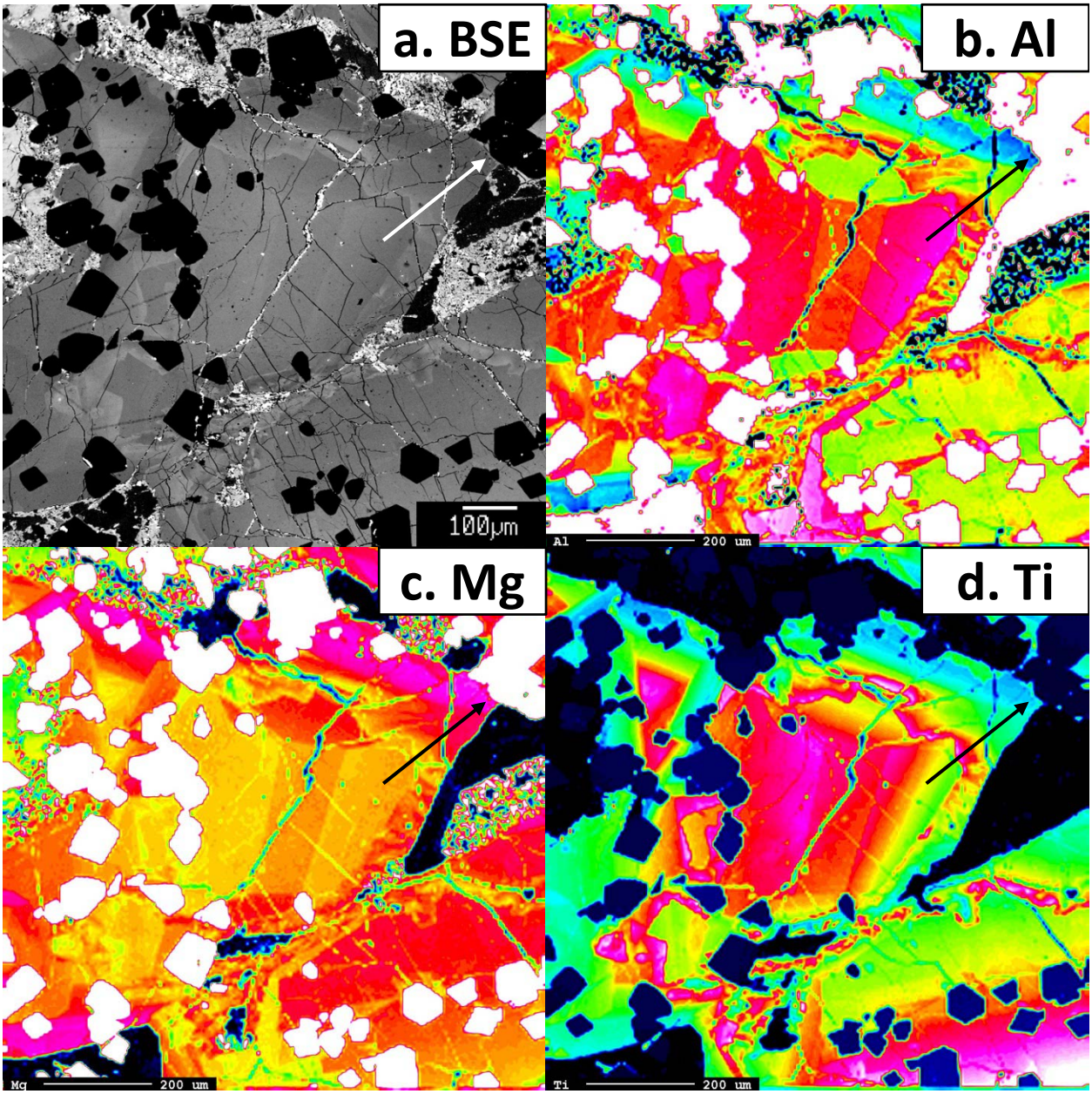

Figure 9.

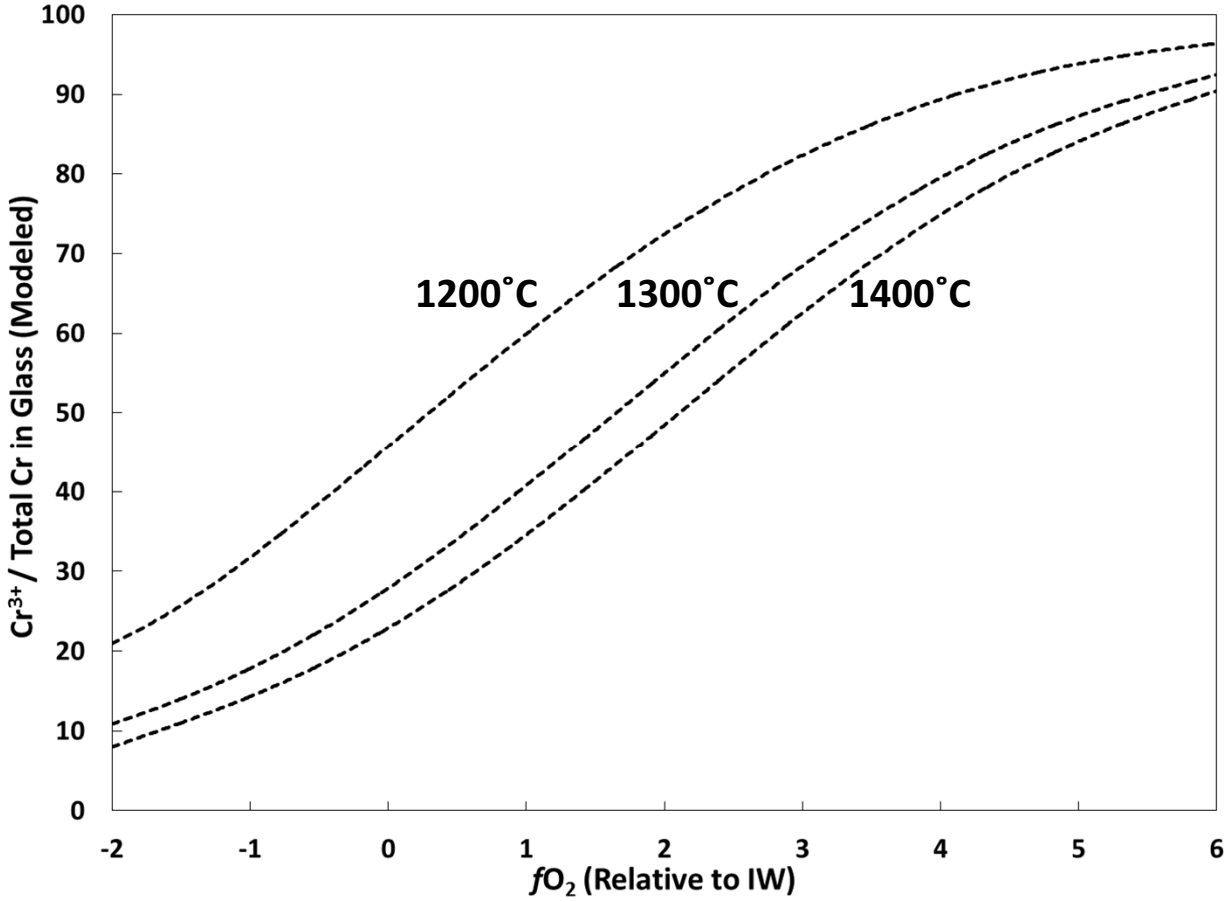
100
90
80
70
60
50
40
30
20
10
0
-2
-1
0
1
2
3
4
5
6
Cr^{3+} / Total Cr in Glass (Modeled)
fO_2 (Relative to IW)
1200˚C
1300˚C
1400˚C

Figure 10.

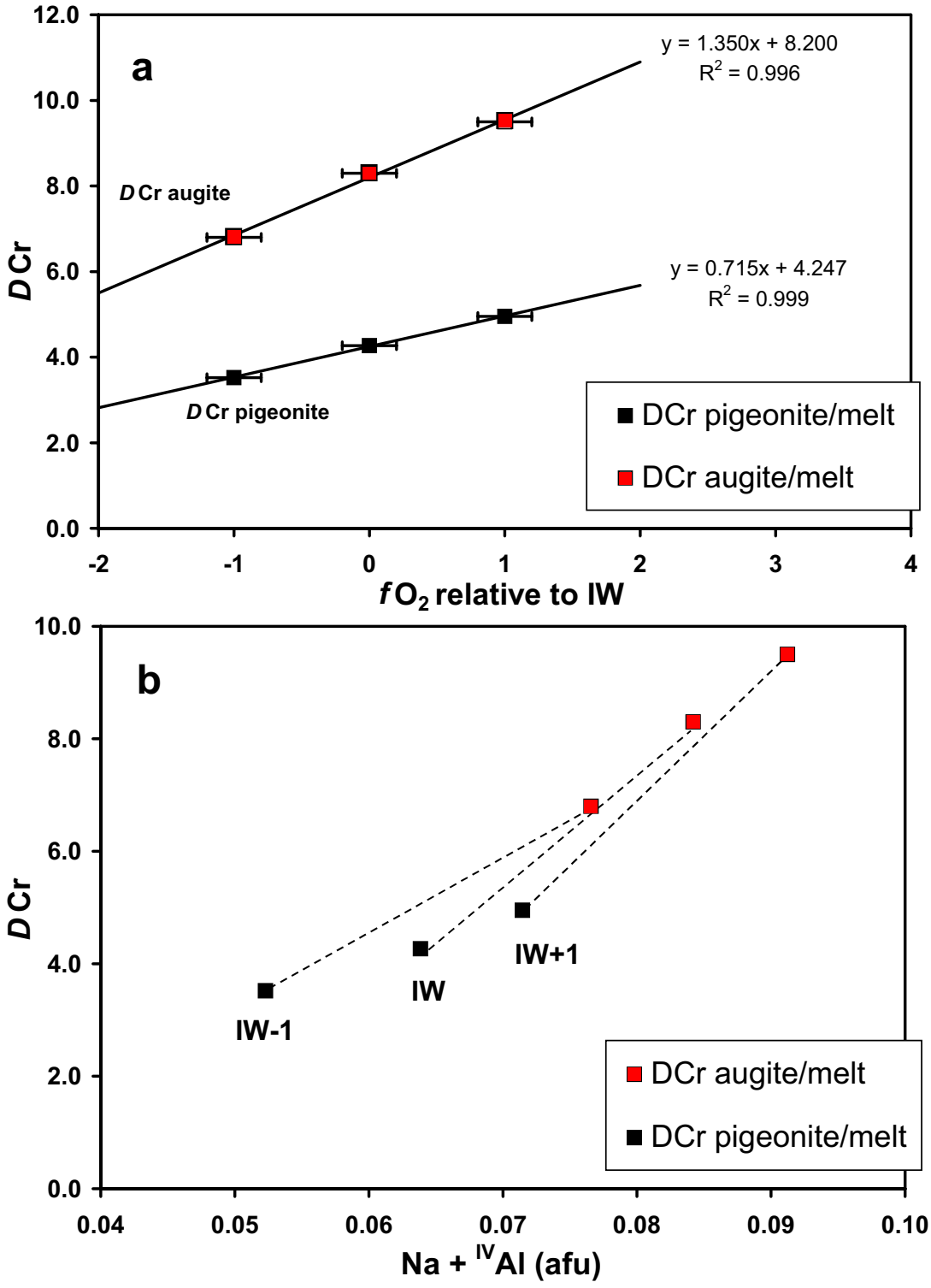
a
y = 1.350x + 8.200
R2 = 0.996
DCr augite
y = 0.715x + 4.247
R2 = 0.999
DCr pigeonite
DCr pigeonite/melt
DCr augite/melt
DCr
fO2 relative to IW
b
IW-1
IW
IW+1
DCr augite/melt
DCr pigeonite/melt
DCr
Na + IVAl (afu)

Figure 11.

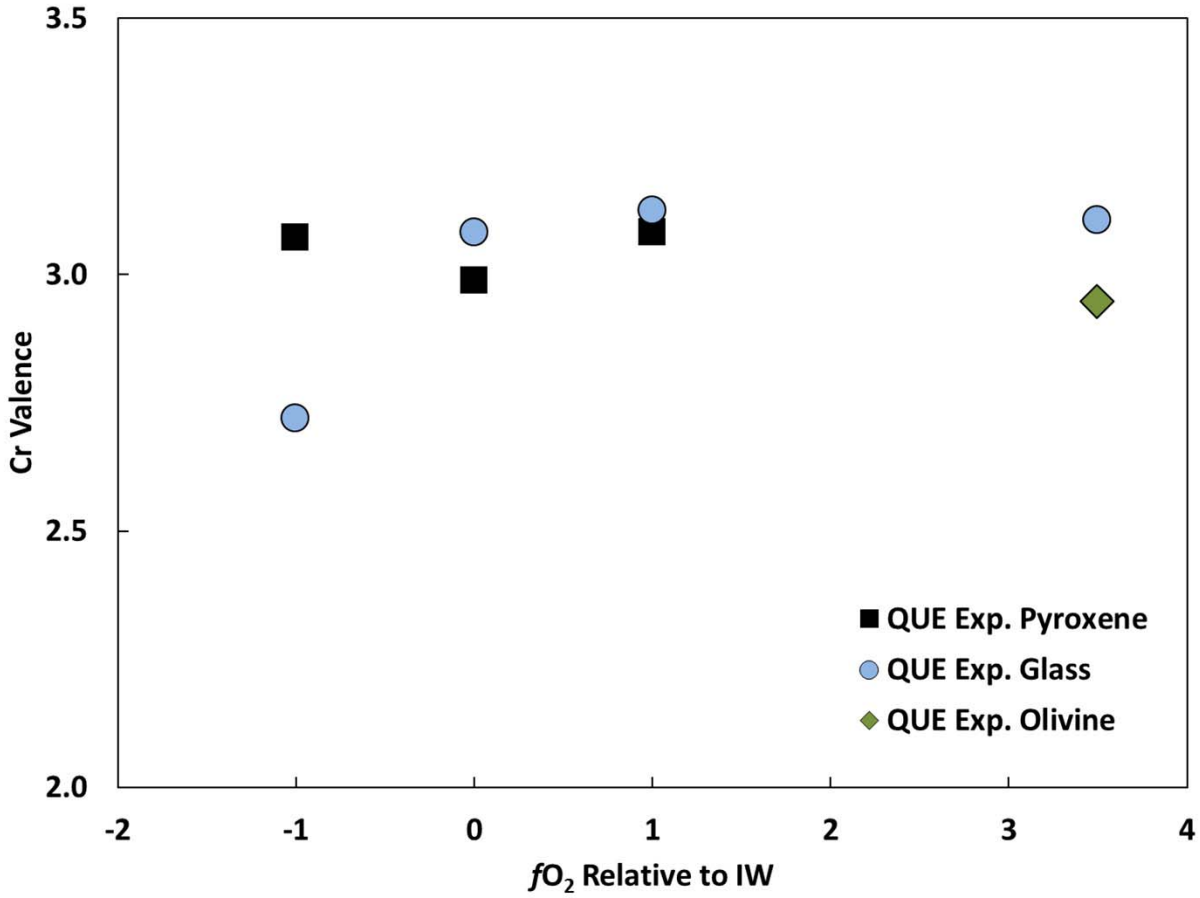
3.5
3.0
2.5
2.0
Cr Valence
-2
-1
0
1
2
3
4
fO_2 Relative to IW
QUE Exp. Pyroxene
QUE Exp. Glass
QUE Exp. Olivine

Figure 12.

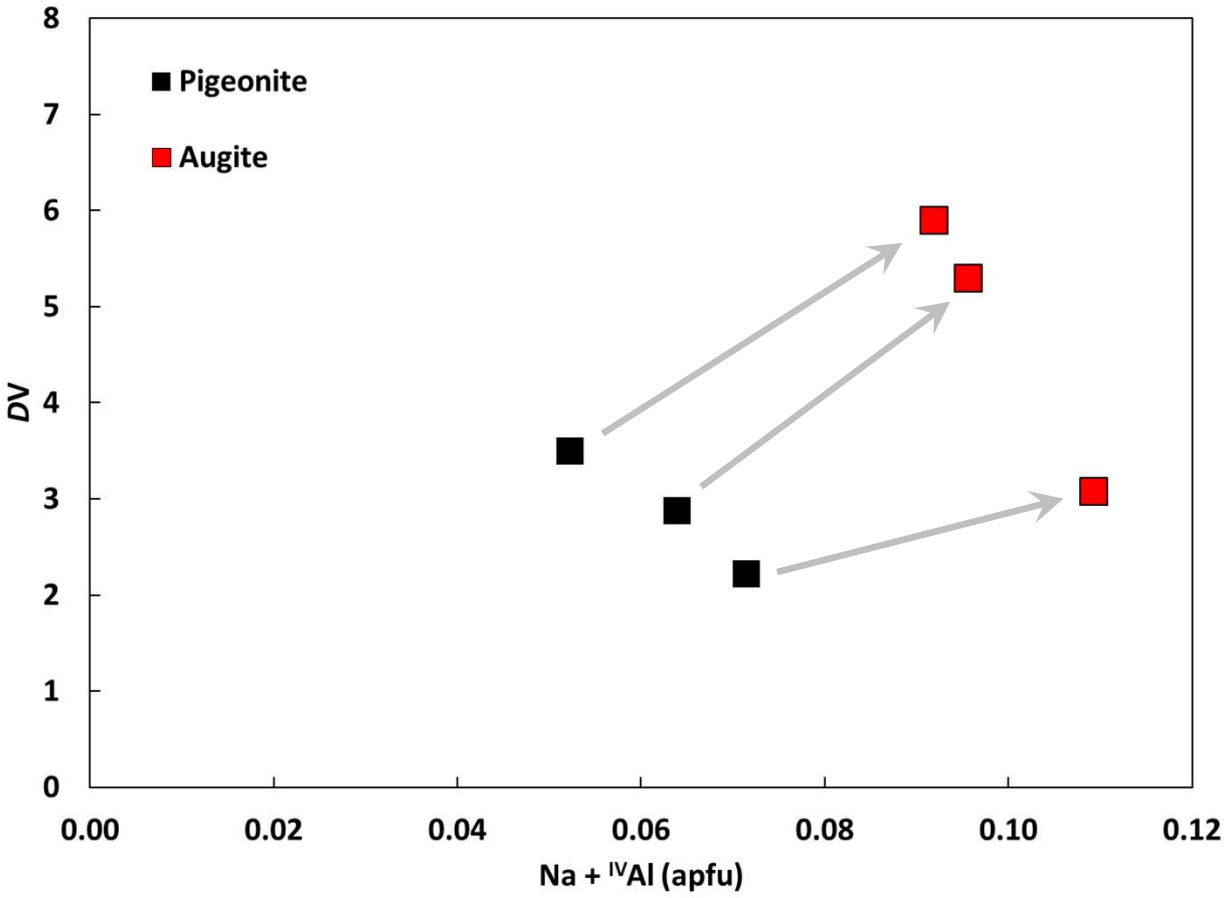
Pigeonite
Augite
DV
Na + IVAl (apfu)
0
1
2
3
4
5
6
7
8
0.00
0.02
0.04
0.06
0.08
0.10
0.12

Figure 13.

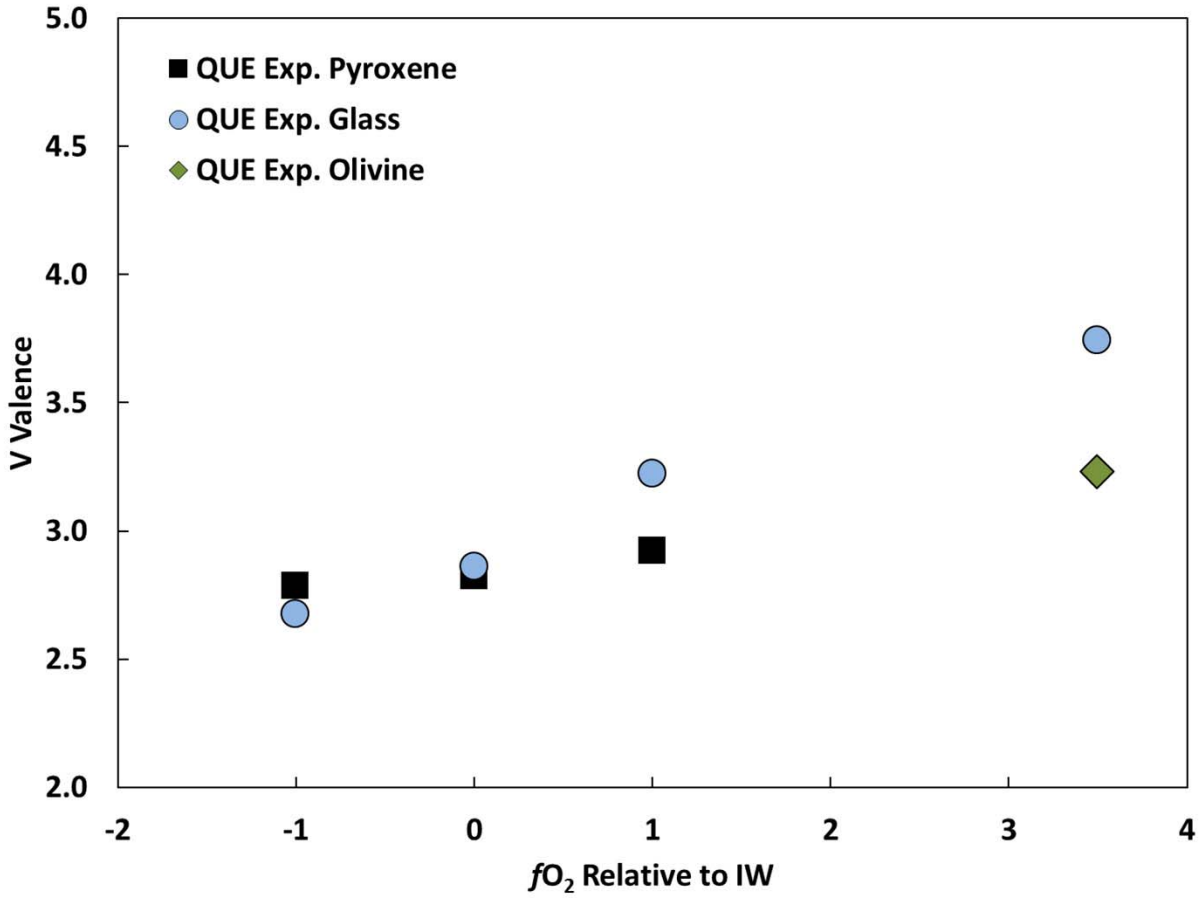
QUE Exp. Pyroxene
QUE Exp. Glass
QUE Exp. Olivine
V Valence
5.0
4.5
4.0
3.5
3.0
2.5
2.0
-2
-1
0
1
2
3
4
fO_2 Relative to IW

Figure 14.

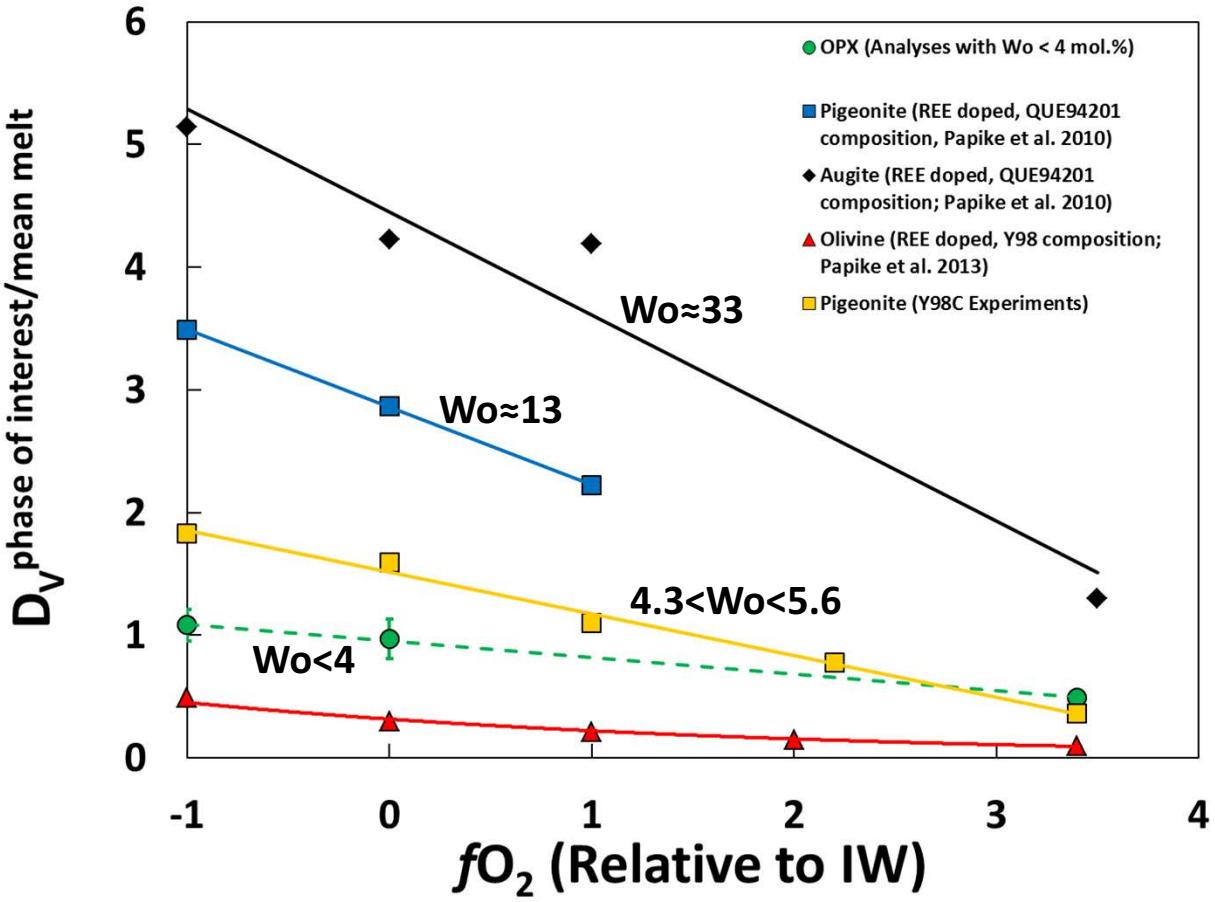
OPX (Analyses with Wo < 4 mol.%)
Pigeonite (REE doped, QUE94201 composition, Papike et al. 2010)
Augite (REE doped, QUE94201 composition; Papike et al. 2010)
Olivine (REE doped, Y98 composition; Papike et al. 2013)
Pigeonite (Y98C Experiments)
Wo≈33
Wo≈13
4.3<Wo<5.6
Wo<4
D_V phase of interest/mean melt
fO_2 (Relative to IW)
0
1
2
3
4
5
6
-1
0
1
2
3
4